J. Fluid Mech. (2003), *vol.* 476, *pp.* 303–334.
DOI: 10.1017/S0022112002002938 Printed in the United Kingdom

Flow past a rotating cylinder

By SANJAY MITTAL AND BHASKAR KUMAR

Department of Aerospace Engineering, Indian Institute of Technology, Kanpur, UP 208 016, India
smittal@iitk.ac.in

(Received 19 July 2001 and in revised form 23 August 2002)

Flow past a spinning circular cylinder placed in a uniform stream is investigated via two-dimensional computations. A stabilized finite element method is utilized to solve the incompressible Navier–Stokes equations in the primitive variables formulation. The Reynolds number based on the cylinder diameter and free-stream speed of the flow is 200. The non-dimensional rotation rate, α (ratio of the surface speed and free-stream speed), is varied between 0 and 5. The time integration of the flow equations is carried out for very large dimensionless time. Vortex shedding is observed for $\alpha < 1.91$. For higher rotation rates the flow achieves a steady state except for $4.34 < \alpha < 4.70$ where the flow is unstable again. In the second region of instability, only one-sided vortex shedding takes place. To ascertain the instability of flow as a function of α a stabilized finite element formulation is proposed to carry out a global, non-parallel stability analysis of the two-dimensional steady-state flow for small disturbances. The formulation and its implementation are validated by predicting the Hopf bifurcation for flow past a non-rotating cylinder. The results from the stability analysis for the rotating cylinder are in very good agreement with those from direct numerical simulations. For large rotation rates, very large lift coefficients can be obtained via the Magnus effect. However, the power requirement for rotating the cylinder increases rapidly with rotation rate.

1. Introduction

Flow past a spinning and translating cylinder has been a subject of numerous investigations. Interest in this flow arises not only from the point of view of understanding wake dynamics but also from its applications to flow control. Tokumaru & Dimotakis (1991, 1993) have demonstrated, via laboratory experiments, that a significant control of the structure of the wake can be achieved by subjecting the cylinder to rotary oscillations. Flow control is also possible by placing rotating cylinders, spinning at constant rate, at appropriate locations in the flow. Modi, Mokhtarian & Fernando (1991) have demonstrated this by controlling flow past airfoils, resulting in a significant increase in the lift. Its application to bluff body flow is useful in drag reduction and suppression of vortex-induced oscillations (Modi 1997).

One of the earliest experiments on flow past a rotating cylinder was carried out by Prandtl (1925). He argued that the maximum lift generated by a spinning cylinder in a uniform flow is limited to 4π (~ 12.6). He also studied the effect of end conditions and aspect ratio. An increase in the overall lift coefficient was observed by utilizing end plates and cylinders of higher aspect ratio. Since then, various studies have been conducted. A fairly comprehensive summary is by Chew, Cheng & Luo (1995). The flow is quite complex despite its simple geometry and various issues regarding this flow remain unresolved even to this date.

One of the issues that remains unresolved is the maximum lift that can be generated by a rotating cylinder placed in a uniform flow. The measurement of lift on a rotating cylinder is quite difficult due to the limitations posed by the rotation of the cylinder. Tokumaru & Dimotakis (1993) devised a method to estimate the mean lift acting on a rotating cylinder in uniform flow. It is based on an inviscid point-vortex model and the transverse velocity that is measured, experimentally, ahead of the cylinder. Their results for $Re = 3.8 \times 10^3$ show that Prandtl's limit on lift coefficient ($C_{Lmax} = 4\pi$) can be exceeded. For example, for $\alpha = 10$ and a cylinder with span to diameter ratio of 18.7, they report an estimated lift coefficient that is more than 20% larger than this limit. Further, the trend of results suggests that C_L can be made larger for higher rotation rates and by taking cylinders of larger aspect ratio. They have suggested that perhaps it is the unsteady effects that weaken Prandtl's hypothesis and that the three-dimensional/end effects are responsible for the increase in the value of lift coefficient compared with that achieved in a purely two-dimensional flow. However, Chew *et al.* (1995) have reported that their two-dimensional computations are in agreement with Prandtl's postulate. They find that for $Re = 1000$, the estimated mean lift coefficient approaches asymptotic values with increase in α. At $\alpha = 6$ they predict a mean lift coefficient of 9.1. Glauert (1957) proposed a solution for a cylinder spinning at high rotation rates where the separation is suppressed. The solution of the flow in the boundary layer is obtained in the form of a power series and an expression for the circulation on the cylinder is obtained. He found that Prandtl's limit can be exceeded and that the circulation increases indefinitely with α. The assumed model for the flow is valid only for those values of α when the flow separation is suppressed.

Most of the other investigations have been limited to $\alpha \leqslant 3.25$. Chen, Ou & Pearlstein (1993) computed flow for $Re = 200$ and $\alpha \leqslant 3.25$. Their computation for $\alpha = 3.25$ does show C_L with instantaneous value exceeding 4π, marginally. However, they report results only for $t \leqslant 24$. Computations by Badr *et al.* (1990) for $\alpha = 3$ and $Re = 1000$ are limited to $t \leqslant 22$. At $t = 22$, C_L is 8.8, approximately, and the trend of their results suggest higher C_L for larger times. The drag coefficient, C_D, reaches almost a steady state value of 5.2. The mean values for C_D and C_L for the fully developed flow reported by Chew *et al.* (1995), for $\alpha = 3$, are 2.8 and 8.7, respectively. Recently, Chou (2000) has also reported computational results for this flow problem. The time histories of C_D and C_L from his computations, for $Re = 1000$ and $\alpha = 3$, match quite well with those from Badr *et al.* (1990) for early times. However, for $t > 5$, he reports much larger values of C_L and smaller values of C_D. It is interesting to observe that the streamline patterns from all the three sets of computations are quite similar and are in good agreement with the flow visualization results. Yet, the discrepancy in the time histories of the aerodynamic coefficients is quite large. Our results for $\alpha = 5$ for various Re, reported in earlier articles (Mittal 2001*a*, *b*), result in large values of C_L. Recently, Stansby & Rainey (2001) have reported computational results for $Re = 200$ and $0 \leqslant \alpha \leqslant 5$. They observe an unsteady flow for lower rotation rates. For high rotation rates a steady flow with very large C_L is realized.

Another question that deserves attention is whether the rotation of cylinder can suppress vortex shedding. Coutanceau & Menard (1985) concluded from their experiments that beyond a critical rotation rate (α_L), following an impulsive start, only one vortex is shed; α_L is almost independent of Re and is about 2. Their view is supported by computations of Badr & Dennis (1985). Diaz *et al.* (1983) also found, via experiments for $Re = 9000$, that the Kármán activity in the wake deteriorates and disappears for α in excess of 2. Chang & Chern (1991) observed vortex shedding in the entire range of $0 \leqslant \alpha \leqslant 2$. However, the Re for their computations ($10^3 \leqslant Re \leqslant 10^6$)

is quite high and the wake is expected to be three-dimensional. Badr *et al.* (1990) carried out investigations, both numerically and experimentally for $10^3 \leqslant Re \leqslant 10^4$ and $\alpha \leqslant 3.0$. Vortex shedding was observed for low α. For larger α, the flow becomes turbulent shortly after the first vortex is released and the flow achieves a steady state. Chen *et al.* (1993) computed flow for $Re = 200$ and $\alpha \leqslant 3.25$. Contrary to the earlier findings, they observed that more than one vortex is shed for $\alpha = 2$ and 3.25. They also found that the vortices shed later are much weaker than the one shed in the beginning. They concluded that the rotation of the cylinder does not suppress vortex shedding for $Re = 200$ and $\alpha = 3.25$. We will show, later in the article, that they were led to this (erroneous) conclusion because they did not compute the flow for a long enough time. Chew *et al.* (1995) found that vortex shedding is suppressed for the $Re = 1000$ flow for $\alpha > 2$. Kang & Choi (1999), from numerical simulations, found that, for $60 \leqslant Re \leqslant 160$, α_L is not constant with Re but shows a logarithmic dependence.

Degani, Walker & Smith (1998) have given a comprehensive account of the work on asymptotic analysis for high-Re flows that involve unsteady separation. They also presented their own results for unsteady boundary development over moving walls using two model problems. One of them is the translating and rotating cylinder. They observed that unsteady separation is delayed with increasing wall speed and is eventually suppressed when the speed of the separation singularity approaches the local mainstream speed. The critical rotation rate, from their computations, at which the shedding disappears ($\alpha_L = 1.91$) is in excellent agreement with the present results for $Re = 200$.

The variation of Strouhal number for vortex shedding, St, with rotation rate for $\alpha < \alpha_L$ is another point of disagreement among the various results in the literature. The results of Chew *et al.* (1995), Diaz *et al.* (1983), Kimura & Tsutahara (1991) and Jaminet & Van Atta (1969) show that St increases with α. However, Hu *et al.* (1996) and Kang & Choi (1999) report that St reduces with α.

The present work is an attempt to resolve some of the issues related to flow past a spinning cylinder in a uniform flow. Most of the results in the literature are for $Re = 200$ and 1000. It is well known that the flow for $Re = 1000$ is highly three-dimensional even for $\alpha = 0$. Therefore, in the present work, the Reynolds number considered is 200. Various spin rates are considered ($0 \leqslant \alpha \leqslant 5$). One of the objectives of the study is to find out the effect of rotation of the cylinder on vortex shedding. This includes finding the α_L for which vortex shedding is completely suppressed. We also investigate the flow for $\alpha > \alpha_L$ to find if there exists a certain range of α where vortex shedding re-occurs. This is motivated by our observations of the changes in the vorticity field as α increases. Perhaps for the first time, it has been found that the cylinder resumes vortex shedding at $\alpha \sim 4.4$ and continues till $\alpha \sim 4.8$. The flow remains stable for higher α. This is confirmed by carrying out a linear stability analysis of the flow. This is another advantage of choosing $Re = 200$. As Re becomes larger, it becomes more difficult to compute a steady-state solution by dropping the unsteady terms from the flow equations, thereby making it increasingly difficult to carry out the linear stability analysis. The modes of shedding for the two regions of instabilities are qualitatively different. In the second region, one-sided shedding is observed. The flows for various α are analysed and a possible cause for the instabilities is proposed.

Results for the mean and fluctuating aerodynamic coefficients for various α are presented. These results also address the issue of whether there exists a C_{Lmax} that can be generated via the Magnus effect. Results on the power required to sustain

the translatory and rotational motion of the cylinder are presented, as well. This information is useful for designing flow control strategies using rotating cylinders.

Preliminary computations have also been carried out for three-dimensional flow past a finite cylinder for various aspect ratios and with different end conditions. It has been observed in experiments that the use of end plates can lead to a substantial increase in lift generated by the cylinder. Our computations show that for $Re = 200$ and $\alpha = 5$ the flow is associated with centrifugal instabilities that exist along the span of the spinning cylinder. Further, in the presence of a 'no-slip' sidewall the flow near the wall separates leading to unsteadiness in the wake. As expected, the effect is more drastic for low-aspect-ratio cylinders. It is the endwall and aspect-ratio effects that limit the lift generated via the Magnus effect. These results will be presented in a future article.

The outline of the rest of this article is as follows. We begin by reviewing the governing equations for incompressible fluid flow in § 2. The problem set-up is defined along with the boundary and initial conditions. Next, the equations for the global, linear stability analysis for the flow equations are presented. The SUPG (streamline-upwind/Petrov–Galerkin) and PSPG (pressure-stabilizing/Petrov–Galerkin) stabilization technique (Tezduyar *et al.* 1992) is employed to stabilize our computations against spurious numerical oscillations and to enable us to use equal-order-interpolation velocity–pressure elements. Section 3 describes the finite element formulation incorporating these stabilizing terms. Also described in the same section is the formulation to carry out the linear stability analysis. This is, perhaps, the first time that a SUPG and PSPG-based stabilized method has been proposed and utilized for conducting computations to assess flow stability. In § 4 computational results for flows involving a rotating cylinder are presented and discussed. First, to validate the present methodology, results are compared with existing results. The results for various α are presented next. The formulation for the stability analysis is checked by determining the point of Hopf bifurcation for flow past a stationary cylinder. This is followed by results from a linear stability analysis for a rotating cylinder. In § 5 a few concluding remarks are made.

2. The governing equations

2.1. *The incompressible flow equations*

Let $\Omega \subset \mathbb{R}^{n_{sd}}$ and $(0, T)$ be the spatial and temporal domains respectively, where n_{sd} is the number of space dimensions, and let Γ denote the boundary of Ω. The spatial and temporal coordinates are denoted by $\boldsymbol{x}$ and t. The Navier–Stokes equations governing incompressible fluid flow are

$$\rho\left(\frac{\partial \boldsymbol{u}}{\partial t} + \boldsymbol{u}\cdot\nabla\boldsymbol{u} - \boldsymbol{f}\right) - \nabla\cdot\boldsymbol{\sigma} = 0 \quad \text{on } \Omega \text{ for } (0, T), \tag{1}$$

$$\nabla\cdot\boldsymbol{u} = 0 \quad \text{on } \Omega \text{ for } (0, T). \tag{2}$$

Here ρ, $\boldsymbol{u}$, $\boldsymbol{f}$ and $\boldsymbol{\sigma}$ are the density, velocity, body force and stress tensor, respectively. The stress tensor is written as the sum of its isotropic and deviatoric parts:

$$\boldsymbol{\sigma} = -p\boldsymbol{I} + \boldsymbol{T}, \quad \boldsymbol{T} = 2\mu\boldsymbol{\varepsilon}(\boldsymbol{u}), \quad \boldsymbol{\varepsilon}(\boldsymbol{u}) = \tfrac{1}{2}((\nabla\boldsymbol{u}) + (\nabla\boldsymbol{u})^T), \tag{3}$$

where p and μ are the pressure and coefficient of dynamic viscosity. Both the Dirichlet and Neumann-type boundary conditions are accounted for, represented as

$$\boldsymbol{u} = \boldsymbol{g} \text{ on } \Gamma_g, \quad \boldsymbol{n}\cdot\boldsymbol{\sigma} = \boldsymbol{h} \text{ on } \Gamma_h, \tag{4}$$

where Γ_g and Γ_h are complementary subsets of the boundary Γ. The initial condition on the velocity is specified on Ω:

$$\boldsymbol{u}(\boldsymbol{x}, 0) = \boldsymbol{u}_0 \quad \text{on } \Omega, \tag{5}$$

where $\boldsymbol{u}_0$ is divergence free.

2.2. *Force and moment coefficients*

The force and moment coefficients are computed by carrying out an integration, that involves the pressure and viscous stresses, around the circumference of the cylinder:

$$C_D = \frac{1}{\frac{1}{2}\rho U^2 2a} \int_{\Gamma_{cyl}} (\boldsymbol{\sigma n}) \cdot \boldsymbol{n}_x \, \mathrm{d}\Gamma, \tag{6}$$

$$C_L = \frac{1}{\frac{1}{2}\rho U^2 2a} \int_{\Gamma_{cyl}} (\boldsymbol{\sigma n}) \cdot \boldsymbol{n}_y \, \mathrm{d}\Gamma, \tag{7}$$

$$C_M = \frac{1}{\frac{1}{2}\rho U^2 2a^2} \int_{\Gamma_{cyl}} (\boldsymbol{\sigma n}) \times (\boldsymbol{r} - \boldsymbol{r}_0) \, \mathrm{d}\Gamma, \tag{8}$$

Here $\boldsymbol{n}_x$ and $\boldsymbol{n}_y$ are the Cartesian components of the unit vector $\boldsymbol{n}$ that is normal to the cylinder boundary Γ_{cyl}, a is the radius of the cylinder, $\boldsymbol{r}$ is the position vector of a point lying on the cylinder surface, $\boldsymbol{r}_0$ is the location of the centre of the cylinder and U the free-stream speed. C_D, C_L and C_M represent the drag, lift and moment coefficient respectively. The contribution of the drag to the power coefficient (C_P) is C_D and that of the moment coefficient is $C_M \omega a/U$ where ω is the rate of rotation of the cylinder.

2.3. *The parameters*

There are two parameters that influence this flow problem: Re and α. The Reynolds number is defined as $Re = 2Ua/v$ where a is the radius of cylinder, U the free-stream speed and v the coefficient of kinematic viscosity of the fluid. The rotation rate of the cylinder is non-dimensionalized with respect to the free-stream speed and is given as $\alpha = a\omega/U$ where ω is the angular velocity of the cylinder about its own axis. All the results presented in this article are with respect to the non-dimensional time $\tau = Ut/a$, where t is the dimensional time.

2.4. *Boundary and initial conditions*

The cylinder resides in a rectangular domain and a flow velocity corresponding to the rotation rate α is specified on the cylinder surface. The rotation is in the counter clockwise direction. The free-stream value is assigned for the velocity at the upstream boundary while at the downstream boundary, a Neumann-type boundary condition for the velocity is specified that corresponds to zero viscous stress vector. On the upper and lower boundaries, the component of velocity normal to and the component of stress vector along these boundaries are prescribed a zero value. The initial condition for all the computations is an impulsive start, i.e. at $t = 0$ the velocity is assigned the value that corresponds to potential flow past a stationary cylinder.

2.5. *Computation of the stream function and vorticity fields*

The present formulation is based on the primitive variables. Once the velocity field is computed, the stream function and vorticity fields are derived from it as post-processing. A finite element formulation based on the least-squares procedure is utilized for the computation.

2.6. *The linear stability flow equations*

To conduct a global, linear stability analysis of a non-parallel flow the unsteady solution is expressed as a combination of the steady solution and the disturbance:

$$\boldsymbol{u} = \boldsymbol{U} + \boldsymbol{u}', \quad p = P + p'. \tag{9}$$

Here, $\boldsymbol{U}$ and P represent the steady-state solution whose stability is to be determined while $\boldsymbol{u}'$ and p' are the velocity and pressure perturbations, respectively. Substituting (9) in (1)–(2) and subtracting the equations for steady flow, one obtains

$$\rho\left(\frac{\partial \boldsymbol{u}'}{\partial t} + \boldsymbol{u}' \cdot \nabla \boldsymbol{U} + \boldsymbol{U} \cdot \nabla \boldsymbol{u}'\right) - \nabla \cdot \boldsymbol{\sigma}' = 0 \quad \text{on } \Omega \text{ for } (0, T), \tag{10}$$

$$\nabla \cdot \boldsymbol{u}' = 0 \quad \text{on } \Omega \text{ for } (0, T). \tag{11}$$

Here, $\boldsymbol{\sigma}'$ is the stress tensor for the perturbed solution computed using (3). We further assume that the disturbances are small and of the following form:

$$\boldsymbol{u}'(\boldsymbol{x}, t) = \hat{\boldsymbol{u}}(\boldsymbol{x})\, \mathrm{e}^{\lambda t}, \tag{12}$$

$$p'(\boldsymbol{x}, t) = \hat{p}(\boldsymbol{x})\, \mathrm{e}^{\lambda t}. \tag{13}$$

Substituting (12)–(13) in (10)–(11) gives

$$\rho(\lambda \hat{\boldsymbol{u}} + \hat{\boldsymbol{u}} \cdot \nabla \boldsymbol{U} + \boldsymbol{U} \cdot \nabla \hat{\boldsymbol{u}}) - \nabla \cdot \hat{\boldsymbol{\sigma}} = 0 \quad \text{on } \Omega, \tag{14}$$

$$\nabla \cdot \hat{\boldsymbol{u}} = 0 \quad \text{on } \Omega. \tag{15}$$

Here, λ is the eigenvalue of the fluid system and governs its stability. In general, $\lambda = \lambda_r + \mathrm{i}\lambda_i$ where, λ_r and λ_i are its real and imaginary parts, respectively. The steady-state solution $(\boldsymbol{U}, P)$ is associated with an unstable mode if the corresponding eigenvalue has a positive real part. The boundary conditions for $\hat{\boldsymbol{u}}$ and $\hat{p}$ are the homogeneous versions of those for U and p as specified by (4).

3. Finite element formulations

Most of the computations reported earlier, for this flow problem, have been carried out using the vorticity/stream-function formulations (Badr *et al.* 1990; Chew *et al.* 1995) or the vorticity/velocity formulations (Chen *et al.* 1993). The present effort employs the finite element formulation of the Navier–Stokes equations in the primitive variables.

3.1. *The incompressible flow equations*

Consider a finite element discretization of Ω into subdomains Ω^e, $e = 1, 2, \ldots, n_{el}$, where n_{el} is the number of elements. Based on this discretization, for velocity and pressure we define the finite element trial function spaces $\mathscr{S}_{\boldsymbol{u}}^h$ and $\mathscr{S}_p^h$, and weighting function spaces $\mathscr{V}_{\boldsymbol{u}}^h$ and $\mathscr{V}_p^h$. These function spaces are selected by taking the Dirichlet boundary conditions into account, as subsets of $[\boldsymbol{H}^{1h}(\Omega)]^{n_{sd}}$ and $\boldsymbol{H}^{1h}(\Omega)$, where $\boldsymbol{H}^{1h}(\Omega)$ is the finite-dimensional function space over Ω. The stabilized finite element formulation of (1)–(2) is written as follows: find $\boldsymbol{u}^h \in \mathscr{S}_{\boldsymbol{u}}^h$ and $p^h \in \mathscr{S}_p^h$ such

that $\forall \boldsymbol{w}^h \in \mathscr{V}_{\boldsymbol{u}}^h$, $q^h \in \mathscr{V}_p^h$

$$\int_\Omega \boldsymbol{w}^h \cdot \rho \left(\frac{\partial \boldsymbol{u}^h}{\partial t} + \boldsymbol{u}^h \cdot \nabla \boldsymbol{u}^h - \boldsymbol{f} \right) \mathrm{d}\Omega + \int_\Omega \boldsymbol{\varepsilon}(\boldsymbol{w}^h) : \boldsymbol{\sigma}(p^h, \boldsymbol{u}^h) \, \mathrm{d}\Omega + \int_\Omega q^h \nabla \cdot \boldsymbol{u}^h \, \mathrm{d}\Omega$$
$$+ \sum_{e=1}^{n_{el}} \int_{\Omega^e} \frac{1}{\rho} \left(\tau_{\mathrm{SUPG}} \rho \boldsymbol{u}^h \cdot \nabla \boldsymbol{w}^h + \tau_{\mathrm{PSPG}} \nabla q^h \right) \left[\rho \left(\frac{\partial \boldsymbol{u}^h}{\partial t} + \boldsymbol{u}^h \cdot \nabla \boldsymbol{u}^h - \boldsymbol{f} \right) - \nabla \cdot \boldsymbol{\sigma}(p^h, \boldsymbol{u}^h) \right] \mathrm{d}\Omega^e$$
$$+ \sum_{e=1}^{n_{el}} \int_{\Omega^e} \tau_{\mathrm{LSIC}} \nabla \cdot \boldsymbol{w}^h \rho \nabla \cdot \boldsymbol{u}^h \, \mathrm{d}\Omega^e = \int_{\Gamma_h} \boldsymbol{w}^h \cdot \boldsymbol{h}^h \, \mathrm{d}\Gamma . \tag{16}$$

In the variational formulation given by (16), the first three terms and the right-hand side constitute the Galerkin formulation of the problem. It is well known that the Galerkin formulation is unstable with respect to the advection operator as the cell Reynolds number (based on the local flow velocity and mesh size) becomes larger. Also, not all combinations of the velocity and pressure interpolations are admissible in the Galerkin formulation. Elements that do not satisfy the Babuska–Brezzi condition lead to oscillatory solutions and, sometimes, no solution at all. To give stability to the basic formulation, a series of element-level integrals are added. The first series of element-level integrals are the SUPG and PSPG stabilization terms added to the variational formulations (Tezduyar *et al.* 1992; Mittal 1992). The terms with τ_{SUPG} as the coefficient render the formulation stable in the presence of advection operator. The term involving τ_{PSPG} allows one to use any combination of velocity and pressure interpolation, including equal-order interpolation. In the current formulation τ_{PSPG} is the same as τ_{SUPG} and is

$$\tau_{\mathrm{SUPG}} = \tau_{\mathrm{PSPG}} = \left(\frac{1}{\tau_{\mathrm{ADV}}^2} + \frac{1}{\tau_{\mathrm{DIF}}^2} \right)^{-1/2}, \tag{17}$$

where

$$\tau_{\mathrm{ADV}} = \frac{h_{\mathrm{UGN}}}{2\|\boldsymbol{u}^h\|}, \quad \tau_{\mathrm{DIF}} = \frac{h_{\mathrm{RGN}}^2}{12\nu}, \tag{18}$$

$$h_{\mathrm{UGN}} = 2 \, \|\boldsymbol{u}^h\| \left(\sum_{a=1}^{n_{en}} |\boldsymbol{u}^h \cdot \nabla N_a| \right)^{-1}, \tag{19}$$

$$h_{\mathrm{RGN}} = 2 \, \|(\nabla \|\boldsymbol{u}^h\|)\| \left(\sum_{a=1}^{n_{en}} |(\nabla \|\boldsymbol{u}^h\|) \cdot \nabla N_a| \right)^{-1}. \tag{20}$$

Here, N_a is the finite element interpolation function and n_{en} is the number of nodes that make up an element. The second series of element-level integrals are added to the formulation for numerical stability at high Reynolds numbers. This is a least-squares term based on the continuity equation. The coefficient τ_{LSIC} is defined as

$$\tau_{\mathrm{LSIC}} = \left(\frac{1}{\delta_{\mathrm{ADV}}^2} + \frac{1}{\delta_{\mathrm{DIF}}^2} \right)^{-1/2}, \tag{21}$$

where

$$\delta_{\mathrm{ADV}} = \frac{h_{\mathrm{UGN}} \|\boldsymbol{u}^h\|}{2}, \quad \delta_{\mathrm{DIF}} = \frac{h_{\mathrm{RGN}}^2 (\|\boldsymbol{u}^h\|)^2}{12\nu}. \tag{22}$$

Both stabilization terms are weighted residuals, and therefore maintain the consistency of the formulation; h is the *element length* and various definitions have been

used by researchers in the past. Mittal (2000) conducted a systematic numerical study to investigate the effect of high-aspect-ratio elements on the performance of the finite element formulation for three commonly used definitions of h. More details on the finite element formulation can be found in the article by Tezduyar *et al.* (1992). In the present work equal-in-order, bilinear, interpolation functions for velocity and pressure have been employed.

The nonlinear equation systems resulting from the finite element discretization of the flow equations are solved using the Generalized Minimal RESidual (GMRES) technique (Saad & Schultz 1986) in conjunction with diagonal preconditioners. The implicit method used in the present work allows us to seek steady-state solutions by simply dropping the unsteady terms in the governing equations.

3.2. *The linear stability flow equations*

Application of the stabilized formulation, as described above, to the equations governing the linear stability results in the following discrete equation:

$$\begin{aligned}
&\int_\Omega \hat{\boldsymbol{w}}^h \cdot \rho \left(\lambda \hat{\boldsymbol{u}}^h + \boldsymbol{U}^h \cdot \nabla \hat{\boldsymbol{u}}^h + \hat{\boldsymbol{u}}^h \cdot \nabla \boldsymbol{U}^h\right) \mathrm{d}\Omega + \int_\Omega \boldsymbol{\varepsilon}(\hat{\boldsymbol{w}}^h) : \boldsymbol{\sigma}(\hat{p}^h, \hat{\boldsymbol{u}}^h)\, \mathrm{d}\Omega \\
&\quad + \int_\Omega \hat{q}^h \nabla \cdot \hat{\boldsymbol{u}}^h \, \mathrm{d}\Omega + \sum_{e=1}^{n_{el}} \int_{\Omega^e} \frac{1}{\rho} (\tau_{\mathrm{SUPG}} \rho \hat{\boldsymbol{u}}^h \cdot \nabla \hat{\boldsymbol{w}}^h \\
&\quad + \tau_{\mathrm{PSPG}} \nabla \hat{q}^h) \cdot \left[\rho(\lambda \hat{\boldsymbol{u}}^h + \boldsymbol{U}^h \cdot \nabla \hat{\boldsymbol{u}}^h + \hat{\boldsymbol{u}}^h \cdot \nabla \boldsymbol{U}^h) - \nabla \cdot \boldsymbol{\sigma}(\hat{p}^h, \hat{\boldsymbol{u}}^h)\right] \mathrm{d}\Omega^e \\
&\quad + \sum_{e=1}^{n_{el}} \int_{\Omega^e} \tau_{\mathrm{LSIC}} \nabla \cdot \hat{\boldsymbol{w}}^h \rho \nabla \cdot \hat{\boldsymbol{u}}^h \mathrm{d}\Omega^e = 0. \qquad (23)
\end{aligned}$$

The formulation given by (23) leads to a generalized eigenvalue problem of the form $\boldsymbol{A}\boldsymbol{X} - \lambda \boldsymbol{B}\boldsymbol{X} = 0$. Both, $\boldsymbol{A}$ and $\boldsymbol{B}$ are sparse matrices. However, $\boldsymbol{B}$ is singular despite the stabilization terms added to the finite element formulation. To overcome this difficulty, the problem is transformed to $\boldsymbol{C}\boldsymbol{X} - (1/\lambda)\boldsymbol{X} = 0$, where, $\boldsymbol{C} = \boldsymbol{A}^{-1}\boldsymbol{B}$. As a result of this transformation we are able to track $1/\lambda$ instead of λ. To check the stability of a steady-state solution we look for the rightmost eigenvalue (having the largest real part), using the subspace iteration method (Stewart 1975). Any flow whose rightmost eigenvalue is negative is stable.

4. Results and discussion

4.1. *Results from two-dimensional computations*

4.1.1. *Comparison with other results*

Flow at $Re = 1000$ past a cylinder with $\alpha = 3.0$ with an impulsive start was computed and instantaneous streamlines for the same parameters were compared with the flow visualization and computational results from Badr *et al.* (1990). These are shown in figure 1. Excellent agreement is observed between the computational results for all times. However, there is some difference between the experimental results and those obtained from computations at larger times ($t = 4$ and 6). In the flow visualization pictures the vortex on the windward side of the cylinder appears to be more fuzzy and located at a smaller angle to the free-stream direction. This discrepancy is perhaps because of the three-dimensionality of the flow and the wake starting to become turbulent. The development of the closed streamlines around the cylinder, with time, can be observed. Flows at $Re = 200$ past a cylinder with $\alpha = 2.07$ and 3.25 with

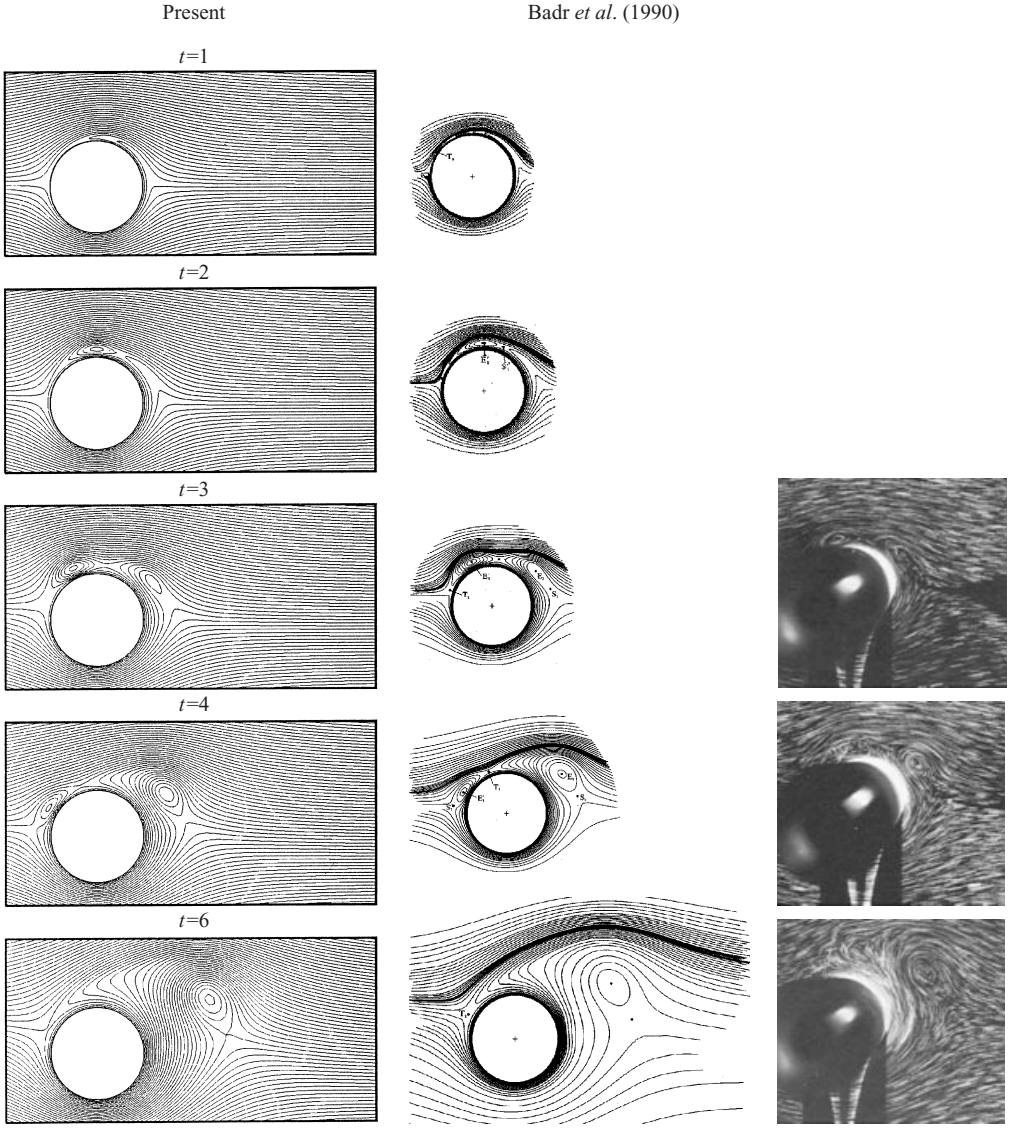

FIGURE 1. $Re = 1000$, $\alpha = 3.0$ flow past a rotating cylinder: comparison of the instantaneous streamline patterns at various time instants from the present computations and those from Badr *et al.* (1990).

an impulsive start were computed and streamlines have been compared with those reported by Chen *et al.* (1993) for the same parameters. All the vortical structures in the flows and their time evolution from the two computations are in very good agreement with each other. The time histories of the lift coefficient for the $Re = 200$ flow are shown in figure 2. The results from the computations of Chen *et al.* (1993) are shown in the same plot. Again, the two results are in very good agreement. This serves as a good check of the present formulation and its implementation for computing flows past rotating cylinders. More comparisons between results from the present formulation and the flow visualization and computational results from Badr *et al.* (1990) for $Re = 1000$ and $\alpha = 0.5$ and 2.0 can be found in our earlier articles (Mittal 2001*a*, *b*).

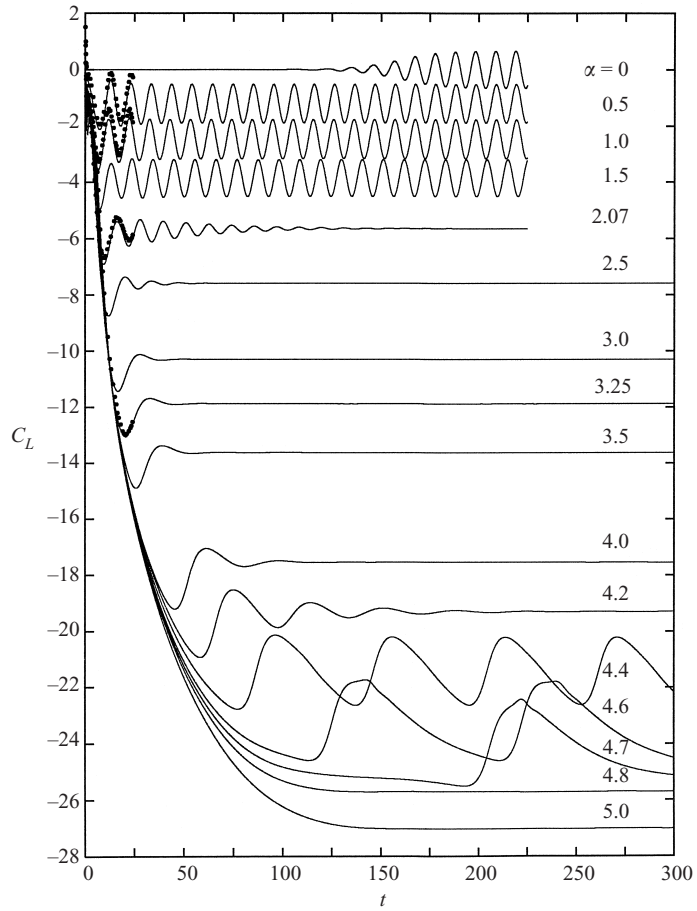

FIGURE 2. $Re = 200$ flow past a rotating cylinder: time histories of C_L for various values of α. Solid symbols (•) are the computational results from Chen *et al.* (1993).

4.1.2. *The finite element mesh*

The mesh used for all the two-dimensional computations consists of 31 800 quadrilateral elements and 32 190 nodes. The cylinder (of diameter D) resides in a computational domain whose outer boundary is a square with edges each located at a distance of L from the centre of the cylinder. There are N_t points in the circumferential direction on the cylinder surface and the radial thickness of the first layer of elements is h_r^1. A close-up view of a typical mesh is shown in figure 3. It can be observed that the mesh is very fine close to the cylinder and the elements become larger with increasing distance from the cylinder. The location of the outer boundary of the domain is expected to become more crucial for larger values of α. It is observed that for $Re = 200$ the flow achieves a steady state for $\alpha = 5.0$. However, $\alpha = 4.5$ is associated with an unsteady solution (see figure 2). To investigate the effect of the location of the outer boundaries of the computational domain a systematic study for various values of L is carried out for the $Re = 200$, $\alpha = 4.5$ flow. Table 1 lists the details for the various meshes that are employed. All the meshes, A1 to A8, have the same distribution of nodes close to the cylinder. The same value of the time step is utilized for computations with all eight meshes. These computations are used to study

Mesh	Nodes	Elements	L/D	h_r^1/D	N_t	Δt
Mesh A1	14 895	14 650	15	0.0025	160	0.025
Mesh A2	16 318	16 056	25	0.0025	160	0.025
Mesh A3	17 880	17 600	37.5	0.0025	160	0.025
Mesh A4	21 512	21 200	50	0.0025	160	0.025
Mesh A5	26 350	26 000	75	0.0025	160	0.025
Mesh A6	32 190	31 800	100	0.0025	160	0.025
Mesh A7	40 440	40 000	125	0.0025	160	0.025
Mesh A8	45 447	44 980	150	0.0025	160	0.025
Mesh A−	19 100	18 800	100	0.005	120	0.025
Mesh A+	64 360	63 800	100	0.0015	200	0.0125

TABLE 1. Details of the various finite element meshes.

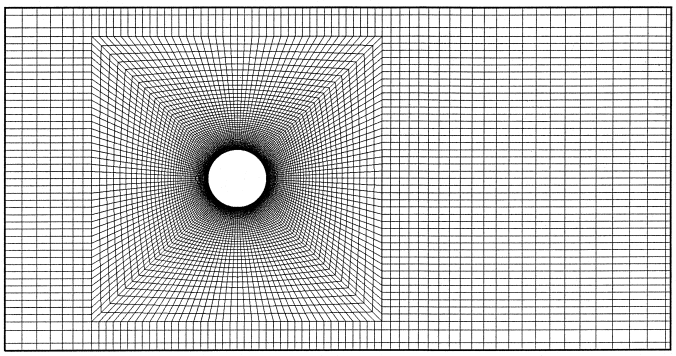

FIGURE 3. $Re = 200$ flow past a rotating cylinder: close-up view of the finite element mesh with 32 190 nodes and 31 800 elements.

the effect of the location of the external boundary by keeping the same spatial and temporal resolutions. The effect of the spatial and temporal resolutions is investigated via computations with meshes A−, A+ and A6 which have the same domain size ($L/D = 100$).

Figure 4 summarizes the results from the convergence study. In all the cases, irrespective of the location of the outer boundary, vortex shedding is observed and the solutions are qualitatively the same. It can be observed that the lift coefficient is fairly insensitive to changes in the mesh or time step. The drag coefficient and the Strouhal number show some dependence on the location of the outer boundaries of the computational domain for $L/D < 75$. However, not much change is observed for L/D larger than 75. The effect of the spatial resolution and time step is also presented in figure 4 for $L/D = 100$. Meshes A6 and A+ produce virtually indistinguishable results. This establishes that the mesh A6 with $\Delta t = 0.025$ and $L/D = 100$ is adequate for computing flows for the present range of α and Re. It was, therefore, decided to carry out the computations in this work with mesh A6 and $\Delta t = 0.025$.

4.1.3. *Overview of the two-dimensional results for various values of* α

For all values of α the flow either achieves a steady state or reaches a temporally periodic solution. Figure 2 shows the time histories of the lift coefficient for the flow past a rotating cylinder for various values of α. The phase diagrams of C_L

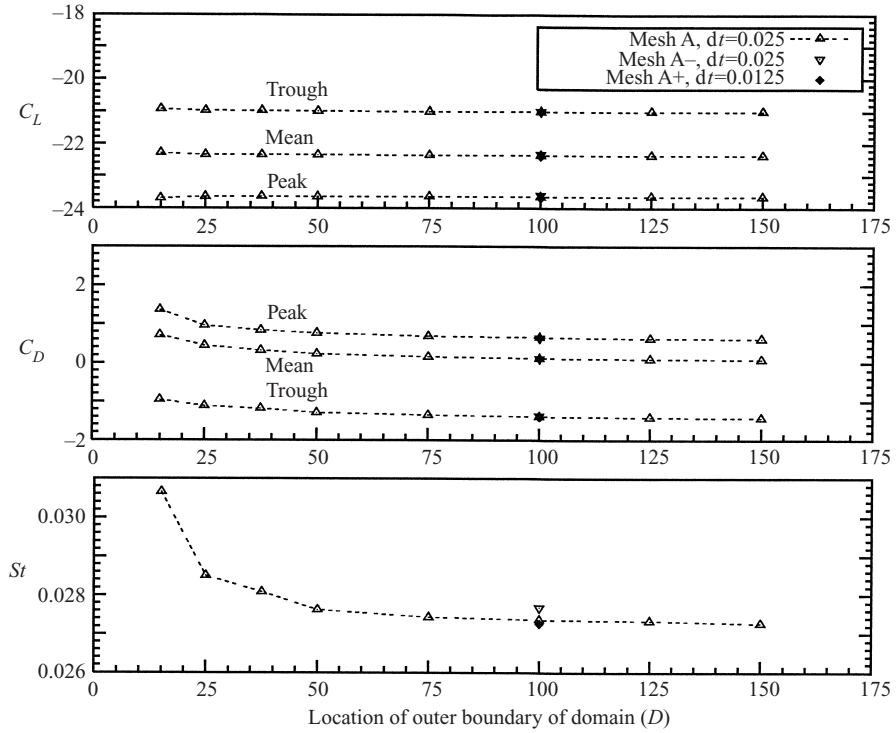

FIGURE 4. $Re = 200$ flow past a rotating cylinder: effect of the location of the outer boundary of the domain with respect to the centre of the cylinder non-dimensionalized with its diameter. Also shown is the effect of mesh refinement for the case when the outer boundary is located at $100D$. Mesh A consists of 32 190 nodes and 31 800 elements while the number of nodes for meshes A+ and A− are 64 360 and 19 100, respectively.

and C_D for the fully developed solution are shown in figure 5. The unsteadiness in the aerodynamic coefficients for the fully developed solution is caused by vortex shedding. While the flow is unsteady for lower values of α, it achieves a steady state for $\alpha \geqslant 1.91$. The vorticity fields for the fully developed solutions are shown in figures 6 and 7. The time instant corresponds to the maximum negative value of the lift coefficient. For the cases that achieve a steady state, the figure shows the fully developed solution. The usual Kármán vortex street is observed for low values of α ($\leqslant 1.9$). A pair of vortices is shed alternately during each cycle of shedding. A clockwise rotating (negative) vortex is shed from the upper surface while a vortex of opposite sense (positive) is released from the lower surface. The flow achieves a temporally periodic state. An increase in the rotation rate is accompanied by an increased upward deflection of the wake and a reduction in its lateral width.

At $\alpha = 1.91$ the vortex shedding ceases and the flow achieves a steady state. This observation is in line with those of other researchers. For example, Kang & Choi (1999) found, via numerical computations, that the critical rotation rate (α_L) at which the shedding disappears is 1.4 for $Re = 60$, 1.8 for $Re = 100$ and 1.9 for $Re = 160$. Diaz *et al.* (1983) observed in their laboratory experiments that the Kármán activity disappears for $\alpha > 2$. The Reynolds number for their experiments is 9000. Chew *et al.* (1995) also observed no shedding beyond $\alpha = 2$ from their computations at $Re = 1000$. Degani *et al.* (1998) carried out an analysis for unsteady boundary layer

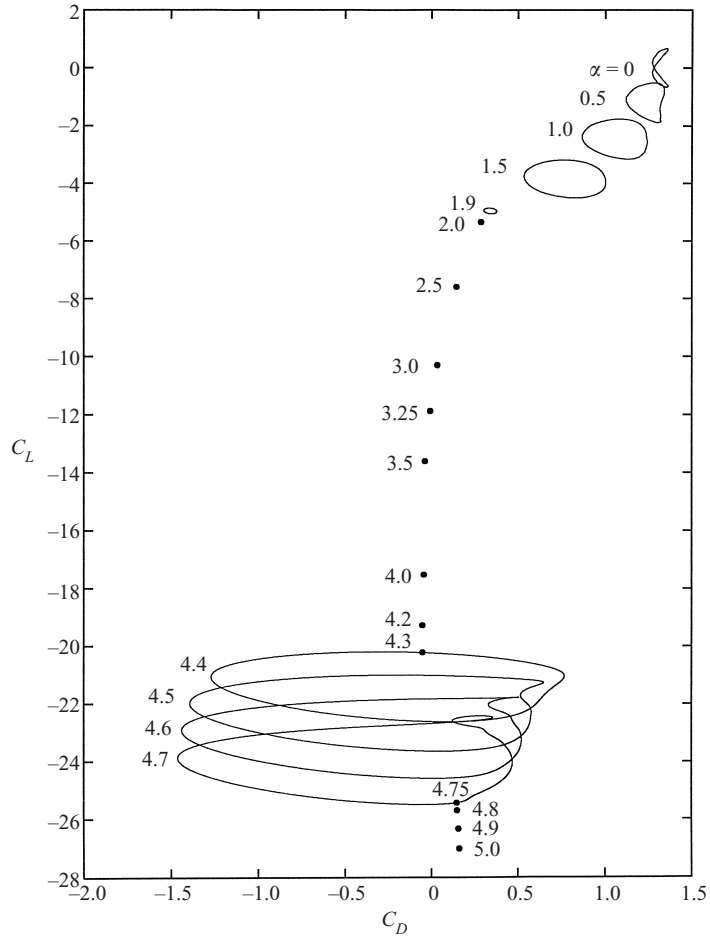

FIGURE 5. $Re = 200$ flow past a rotating cylinder: phase diagrams of C_L and C_D for various values of α.

development over moving walls in the limit of infinite Reynolds numbers. In their study, no unsteady separation was detected for α beyond 1.91.

Most researchers in the past have not investigated the flow for values of α much larger than α_L (the critical value beyond which the vortex shedding ceases). In the present work α is varied between 0 and 5 for $Re = 200$. It is seen that the flow remains steady for $1.91 \leqslant \alpha \leqslant 4.35$. However, the flow is unstable again for $4.34 < \alpha < 4.75$. This second instability appears to be stronger than the first one from the point of view of the amplitude of the unsteady component of aerodynamic forces acting on the cylinder. This is, perhaps, the first time that a small window of α has been observed in this regime where this flow exhibits an instability. Beyond $\alpha \geqslant 4.75$ the flow is steady, but multiple solutions are observed. The set of solutions obtained by initiating the computations with an impulsive start result in stable flow. These solutions are identical to those obtained by starting from a stable flow for $\alpha = 5$ and then by decreasing α. The solutions computed by increasing α and starting from a solution for $\alpha \leqslant 4.7$ are unstable. This is expected to have significant implications for flow control using rotation of cylinders.

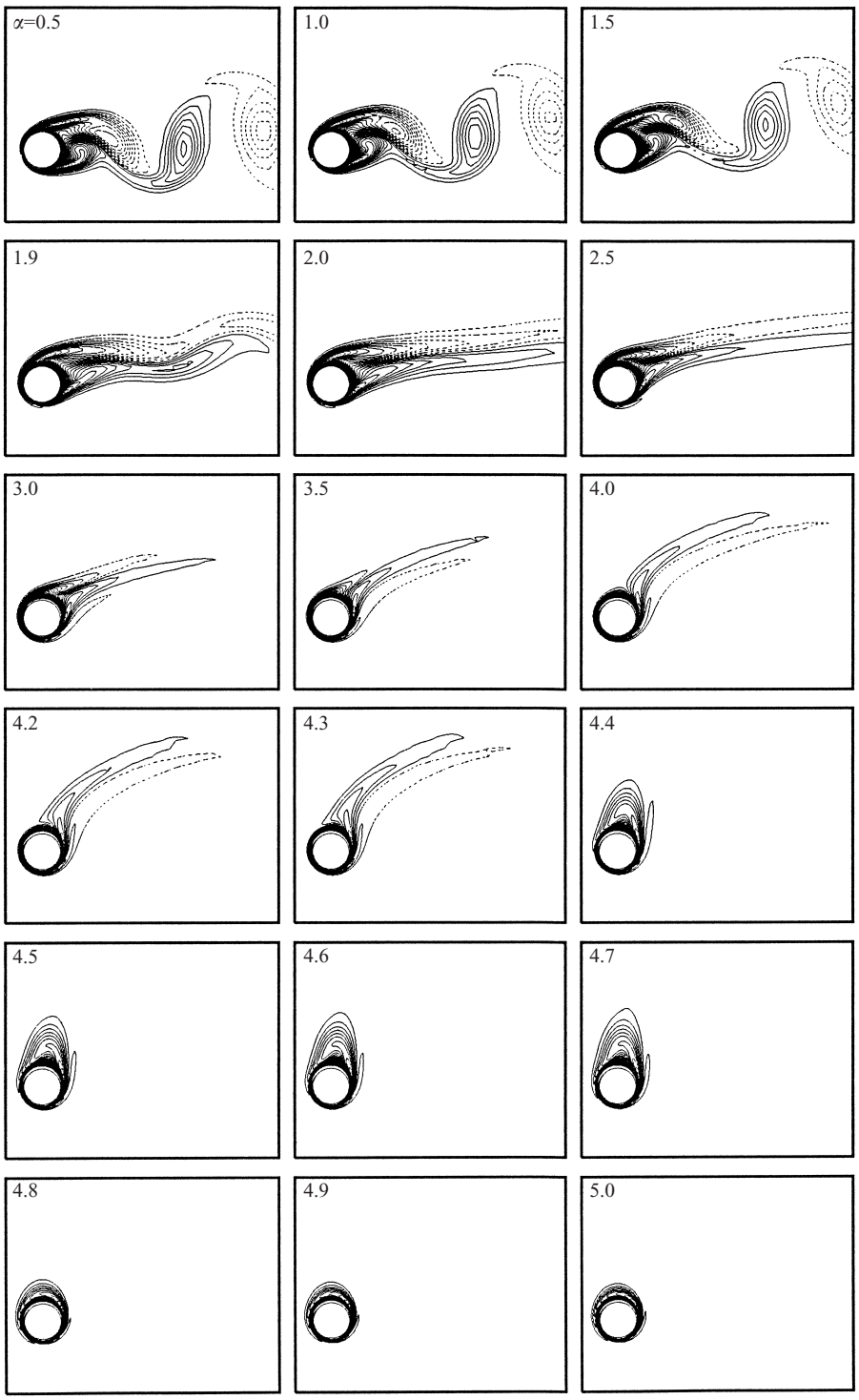

FIGURE 6. $Re = 200$ flow past a rotating cylinder: close up view of the vorticity field for the fully developed solution at various values of α. For the cases that exhibit a temporally periodic solution, the time instant at which the picture is shown corresponds to the lift coefficient having the largest magnitude. Solid lines denote positive while broken lines show negative vorticity.

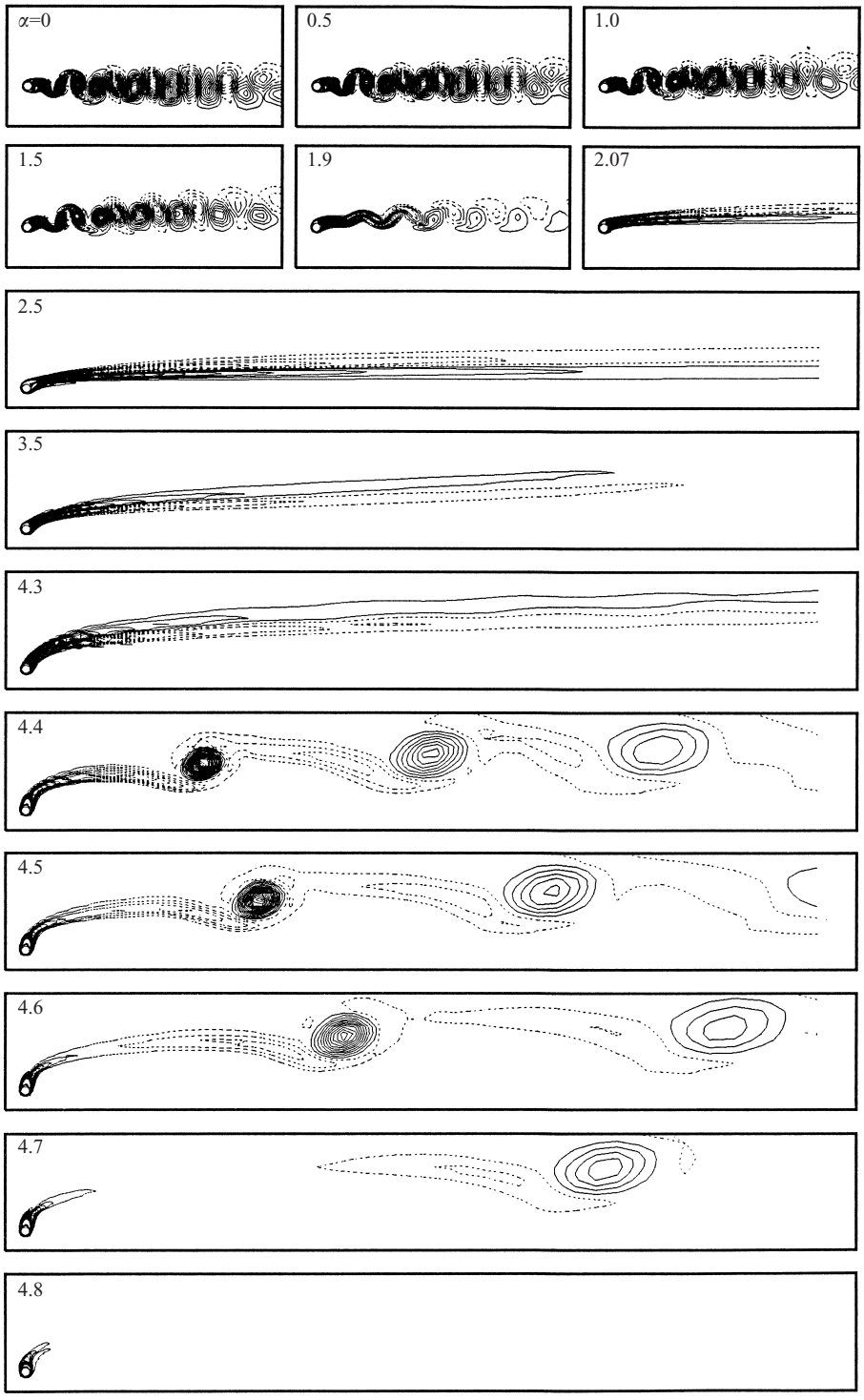

FIGURE 7. $Re = 200$ flow past a rotating cylinder: global view of the vorticity field for the fully developed solution at various values of α. For the cases that exhibit a temporally periodic solution, the time instant at which the picture is shown corresponds to the lift coefficient having the largest magnitude.

4.1.4. *Flow for* $\alpha \leqslant 2$

The inviscid analysis for $\alpha < 2$ predicts a steady flow with two stagnation points that lie on the surface of the cylinder. The viscous flow is quite different from the inviscid one. Neither the flow is steady, nor do the stagnation points lie on the surface of the cylinder. Since the speed on the cylinder surface is constant, unlike potential flow, closed streamlines are observed near the surface even for low values of α.

The phase plot of C_L vs. C_D resembles a figure of 8 for $\alpha = 0$. A vortex is released from each of the upper and lower surfaces of the cylinder during every cycle of shedding. The two vortices are of equal strength and the frequency of drag variation is twice that of the variation of lift. The clockwise rotating vortex is more or less restricted to the upper portion of the cylinder in the near wake. Similarly, the counter-clockwise rotating vortex occupies the lower half of the cylinder. The computations result in $St = 0.1934$ and $\overline{C}_D = 1.316$. (Here, Strouhal number $St = f2a/U$, where f is the vortex shedding frequency.) These values are in excellent agreement with the experimental and numerical data reported by other researchers. For example, measurements by Williamson (1991) show $St = 0.196$ for this flow.

Rotation of the cylinder introduces asymmetry in the strength and location of the positive and negative vortices. Additionally, some of the vorticity generated on the rotating cylinder appears to be wrapped around it. It can be seen from figures 6 and 7 that the clockwise vorticity generated on the windward side of the spinning cylinder protrudes beyond the x-axis like a 'tongue'. Similarly, on the leeward side, the region of counter-clockwise vorticity extends a 'tongue' upwards, along the cylinder. The length of these vortical structures increases with spin rate. At very high spin rates (for example, $\alpha = 5$) these two regions of vorticity go around the cylinder as tightly wound spirals. Similar results are obtained from the plots of steady-state flows. These are obtained by dropping the unsteady terms from the governing flow equations. Vorticity fields for these solutions are shown in figure 8. Multiple steady states are observed for $\alpha \geqslant 4.8$. One set of solutions shown in figure 8(a) are obtained by increasing α. The solution obtained this way is observed to be different from that computed via unsteady computations following an impulsive start. The $\alpha = 5$ flow, obtained via unsteady computations, is utilized to compute flows for lower rotation rates by decreasing α. The solutions obtained in this manner are shown in figure 8(b). Note that the steady-state solutions computed by the two methods are identical for $\alpha \leqslant 4.7$.

Figure 9 shows the vorticity distribution on the cylinder surface for the steady-state solutions. The changes in the variation of surface vorticity with spin rate are more drastic on the upper surface of the cylinder than on the lower surface. Compared to $\alpha = 0$ the maximum value of the vorticity, both positive and negative, first decreases and then increases. The peak value of the positive vorticity, for all rotation rates, is roughly at the same location on the lower surface of the cylinder. However, the location of the peak value of negative vorticity varies very significantly with α. For zero spin the maximum value is observed on the windward side (at $\theta \sim 130^\circ$). For $\alpha = 1.0$ a new peak starts to form at a location on the leeward side which is almost diametrically opposite ($\theta \sim -50^\circ$). The maximum value is still at about the same location, although its magnitude reduces. At $\alpha = 2.0$ this new local peak becomes a global maximum and is located at $\theta \sim -20^\circ$. It is, perhaps, this redistribution of surface vorticity that gives stability to the flow for α larger than 1.9. More will be said on this later.

Shown in figure 10 is the coefficient of pressure distribution on the cylinder surface for the steady-state solutions for various α. For $\alpha = 0$, the C_p distributions on the

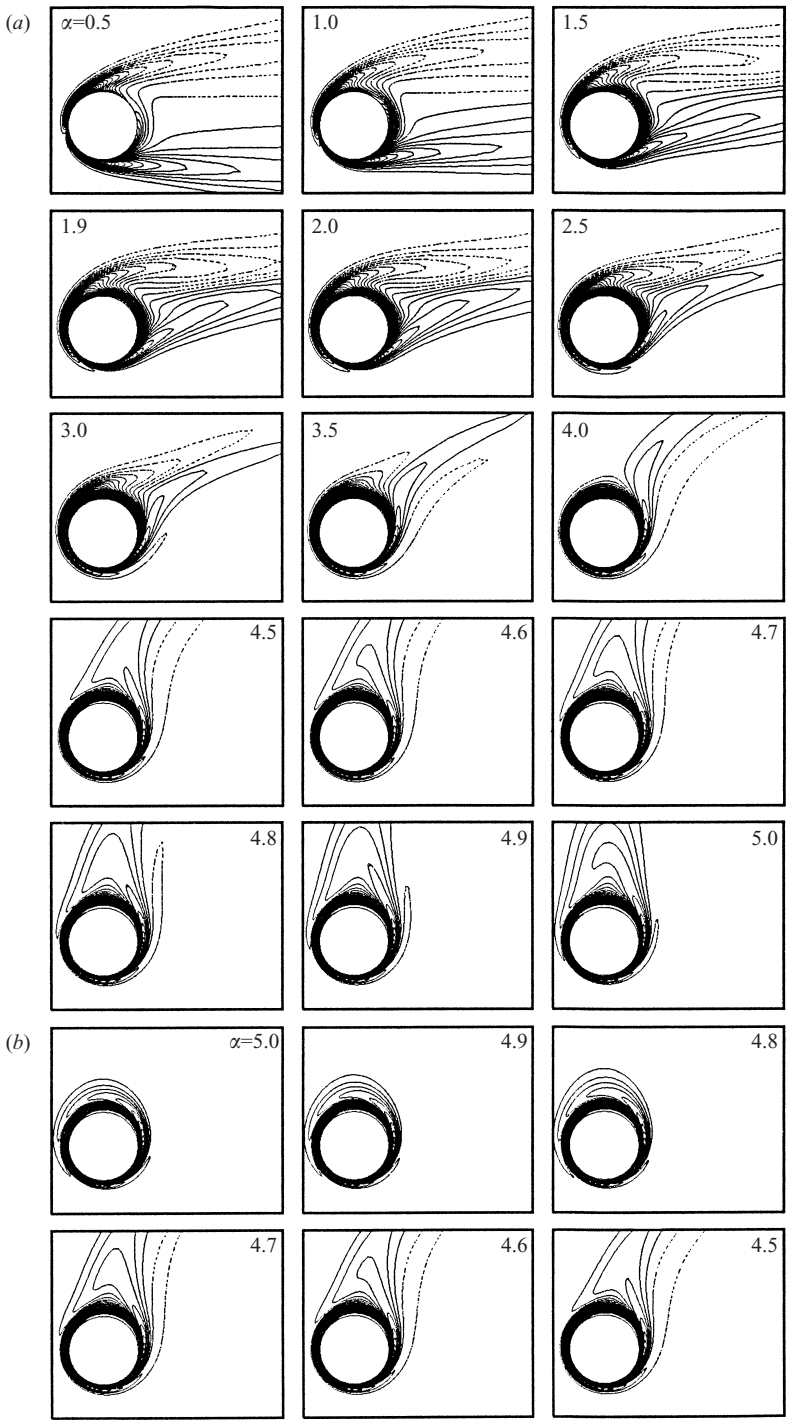

FIGURE 8. $Re = 200$ flow past a rotating cylinder: vorticity field for the steady-state solution at various values of α computed by dropping the unsteady terms in the governing equations. (*a*) Increasing α and with computations initiated with $\alpha = 0$. (*b*) Decreasing α and with computations initiated with the solution obtained from two-dimensional DNS for $\alpha = 5$.

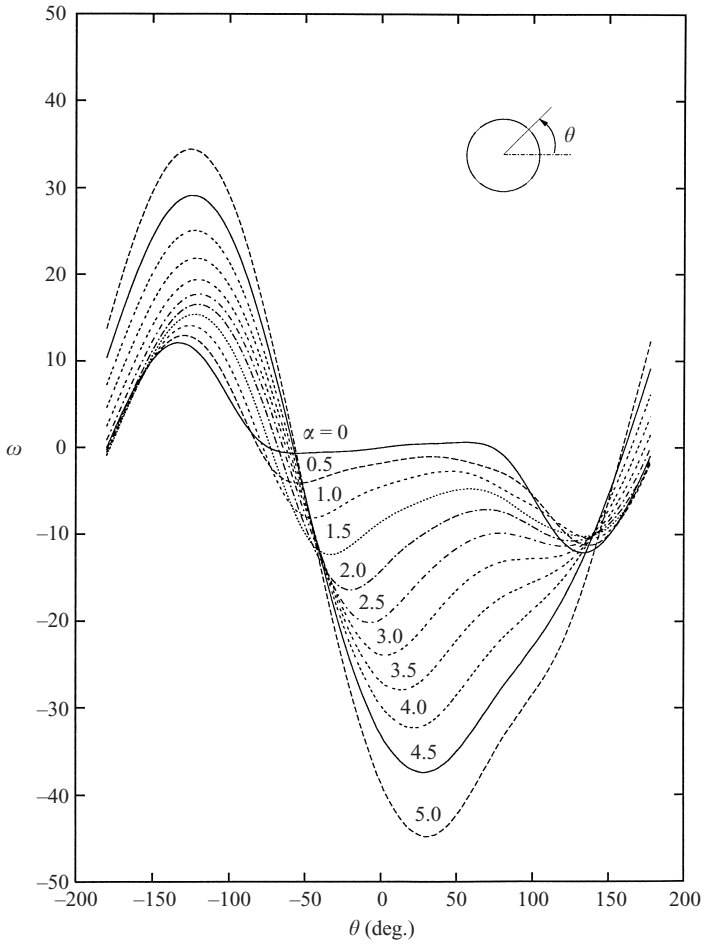

FIGURE 9. $Re = 200$ flow past a rotating cylinder for various α: variation of vorticity on the surface of the cylinder for the steady-state solution.

leeward side of the cylinder for the inviscid and $Re = 200$ flows are qualitatively different. In the viscous case, the flow separates and an almost constant pressure is observed on the rear of the cylinder. For higher spin rates, the C_p distribution is qualitatively similar to that observed in the inviscid flow. For example, in figure 10, the C_p distribution from the potential flow theory is shown for $\alpha = 4$. Although the peak suction generated in the inviscid flow is significantly higher, the general behaviour in the two cases is very similar. It is also interesting to observe from the figure that the C_p distribution for the inviscid flow is symmetric about $\theta = \pi/2$. This results in zero drag. However, this is not the case for the $Re = 200$ flow. For higher rotation rates, the C_p on the windward side is larger than that on the leeward side of the cylinder and this results in generation of thrust. This is also seen from figure 11. The viscous effects contribute to the drag force and result in a net drag on the cylinder for most values of α. For $3.2 < \alpha < 4.3$ the cylinder experiences a very small net thrust. However, the power needed to rotate the cylinder is still fairly large.

Figure 11 shows a summary of the variation with α of the aerodynamic coefficients for the cylinder. It is interesting to observe that the mean values of the lift and

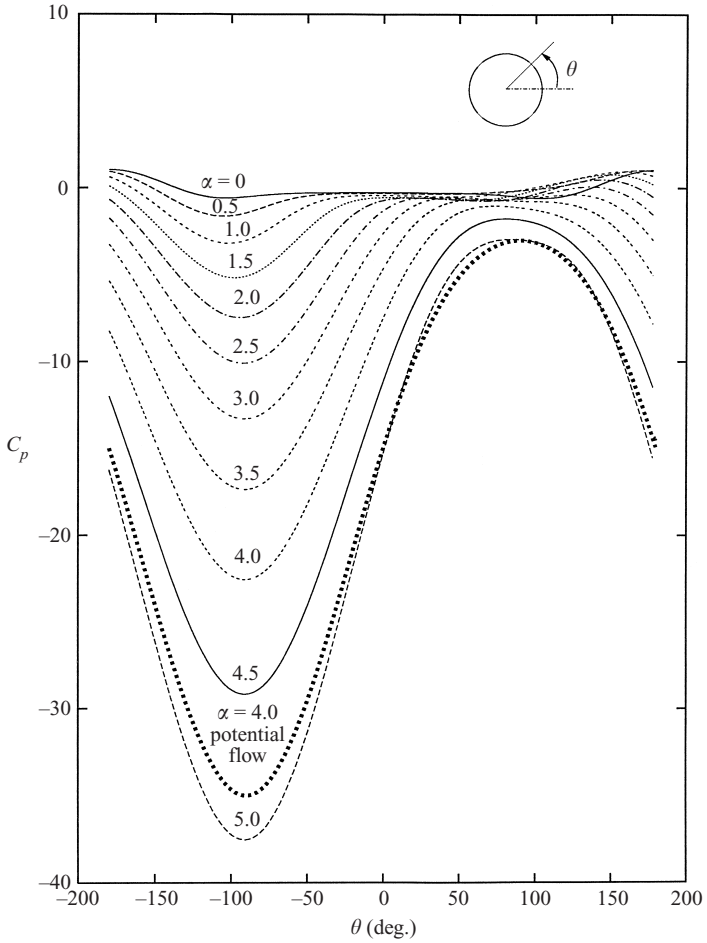

FIGURE 10. $Re = 200$ flow past a rotating cylinder for various α: variation of pressure coefficient on the surface of cylinder for the steady-state solution. The thick broken line shows the C_p distribution for potential flow for $\alpha = 4.0$.

drag coefficients from the unsteady flows are different from the values obtained from the steady-state computations. Compared to C_L, C_D appears to be more sensitive to unsteadiness. Perhaps this is because the drag coefficient is substantially smaller in magnitude than the lift coefficient. Therefore, unlike C_L, small changes in C_D may appear as large percentage changes. The power coefficient, C_P, increases rapidly with α. This suggests that lift generation by the Magnus effect is an expensive proposition, especially, for large values of C_L. The unsteadiness in the flow, as suggested by the r.m.s. values of C_L and C_D are maximum at $\alpha = 1.5$, approximately.

Also shown in figure 11 is the mean lift generated by the cylinder for various rotation rates from the potential flow theory and that due to Glauert (1957). The present results clearly indicate that Prandtl's limit of $(C_L)_{max} = 4\pi$ is exceeded for large α. The results from the present computations compare quite well with the high-α theory proposed by Glauert (1957). Also, the variation of $\overline{C}_L$ with α is closer to the potential flow results for large α. This is consistent with our earlier observation about the similarity of pressure distributions for the viscous and inviscid flows for large α. Our computations indicate that the lift generation is primarily due to pressure variations.

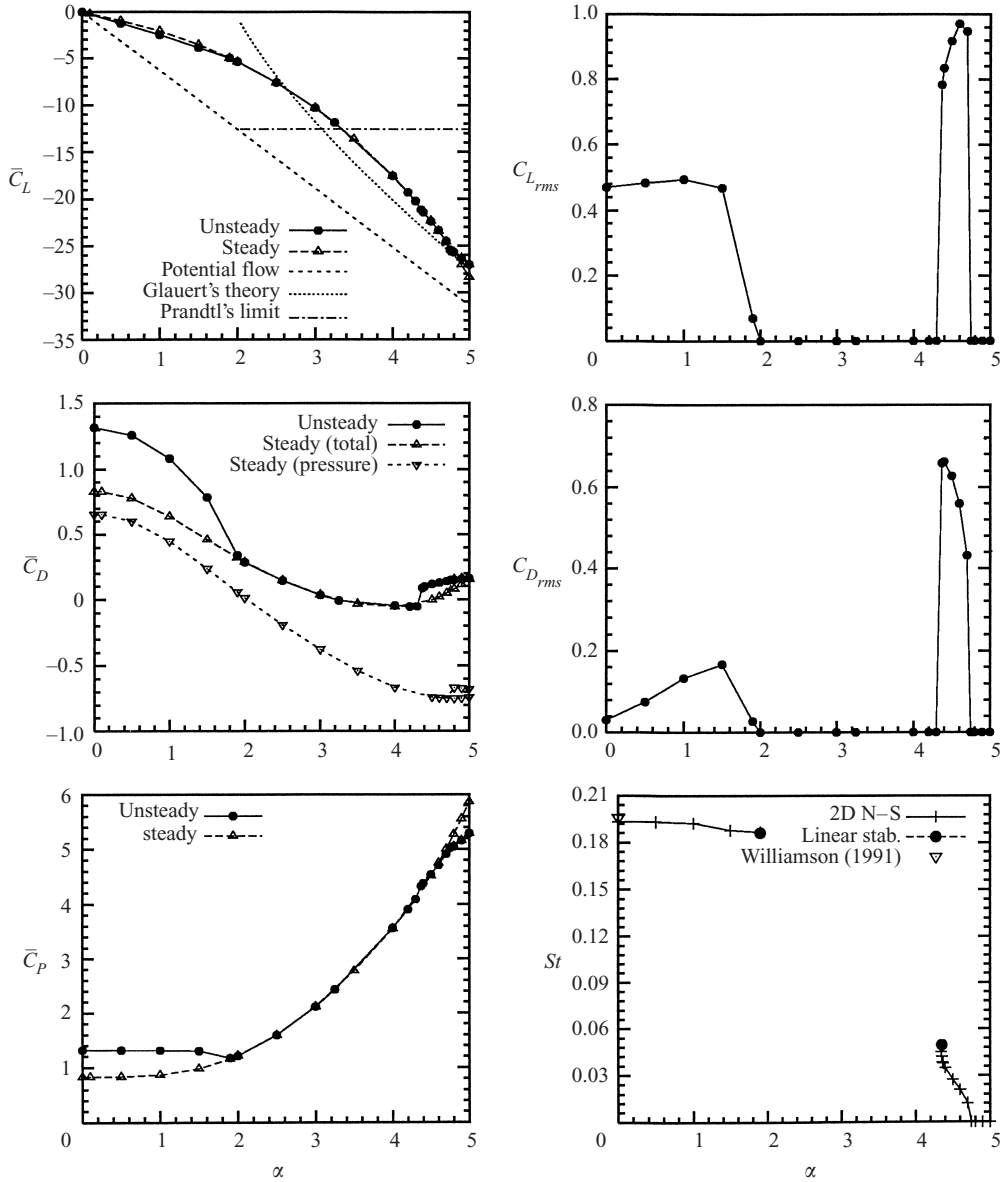

FIGURE 11. $Re = 200$ flow past a rotating cylinder: variation of the time-averaged and r.m.s. values of the lift and drag coefficients, power coefficient and Strouhal number with rotation rate. The plots on the left show the time-averaged quantities for the unsteady simulations as well as the values obtained with the steady-state computations by dropping the unsteady terms in the governing equations. Also shown is the Strouhal number for the most unstable mode obtained with the linear stability analysis at the onset of shedding.

The contribution from the viscous forces is negligible. It should be pointed out that the velocity profiles, close to the cylinder surface, from the present computations and from the theory proposed by Glauert (1957) do not match very well. This might be because the Reynolds number in the present computations is not high enough to be compared with the asymptotic analysis at high *Re*. The lift coefficients result in a good

match because the main contribution is from the pressure variation; contributions due to shear stresses are negligible.

The flow goes through a qualitative change as α passes through the value of 1. This has also been pointed out by Diaz *et al.* (1983). For $\alpha = 0$ the speeds on the lower and upper surfaces of the cylinder are same. For $\alpha < 1$ the speed on the lower surface of the cylinder is smaller than the free-stream speed. It matches the free-stream speed for $\alpha = 1$. For $\alpha > 1$ the surface speed on the lower part of the cylinder exceeds the free-stream speed. The disparity between the flows on the upper and lower surfaces of the cylinder increases with α.

Figure 5 indicates that the vortex shedding ceases beyond $\alpha \sim 1.9$. For $\alpha < 1.9$ the Strouhal number decreases with increase in α. All the earlier computational studies, except the results of Chew *et al.* (1995), report a similar trend. Computational results from Kang & Choi (1999) for $Re = 160$ show a decrease in St with increasing α. The same trend is reported by Hu *et al.* (1996) via a low-dimensional Galerkin method for $Re = 60$. On the other hand, Chew *et al.* (1995) find that St increases with α for $Re = 1000$. The experiments of Diaz *et al.* (1983) for $Re = 9000$ and Kimura & Tsutahara (1991) for $Re = 280$ and 370 show an increase in the Strouhal number with rotation rate. Van Atta (1997) has pointed out that Hu's (1996) results are in conflict with earlier experimental results (Jaminet & Van Atta 1969). It appears that the experiments and computations show an exactly opposite trend in the St vs. α relationship. This difference remains unresolved and is, perhaps, related to the interaction between the vortex-shedding and centrifugal instabilities that might exist for such flows. It would be interesting to carry out three-dimensional computations for this flow for $\alpha < 2$. What adds credibility to the present set of results is the fact that for $\alpha = 1.91$ the value of St matches that obtained from the global, linear stability analysis of the flow. This is also shown in figure 11. For $\alpha = 0$, the St matches very well with the data from Williamson (1991). In addition, the trend of variation of St with α is consistent with the observation that the wake narrows with increase in rotation rate. The reduction in the lateral width of the wake implies that the shear layers are closer to each other. A shorter characteristic length, from simple physical arguments, suggests larger time scales for shedding.

4.1.5. *Flow for* $\alpha = 3.07$

One of the objectives of the present work is to address the question of whether or not cylinder rotation can suppress vortex shedding. Chen *et al.* (1993) carried out computations for $Re = 200$ and $\alpha = 3.25$. They continued their computations with the base mesh till $t = 24$ and then with the stretched grid till $t = 54$. The time histories for lift and drag have been reported for $t \leqslant 24$. Based on their observations they concluded that vortex shedding persists for $\alpha = 3.25$. This is in contrast to the earlier conclusion by Coutanceau & Menard (1985) based on flow-visualization studies. No other long time results for these flow parameters exist in the literature to allow a definite conclusion.

Our computational results are in agreement with those of Chen *et al.* (1993) for the duration of their computations. This can be seen from the time histories for lift coefficient shown in figure 2. As far as the fully developed solution is concerned, it is clear from figure 2 that the flow takes a long time to achieve a fully developed state. Chen *et al.* (1993) did not compute the flow for long enough and concluded, incorrectly, that the flow does not reach a steady state. The vorticity fields at various time instants for the simulation are shown in figure 12. Clearly, vortical activity is

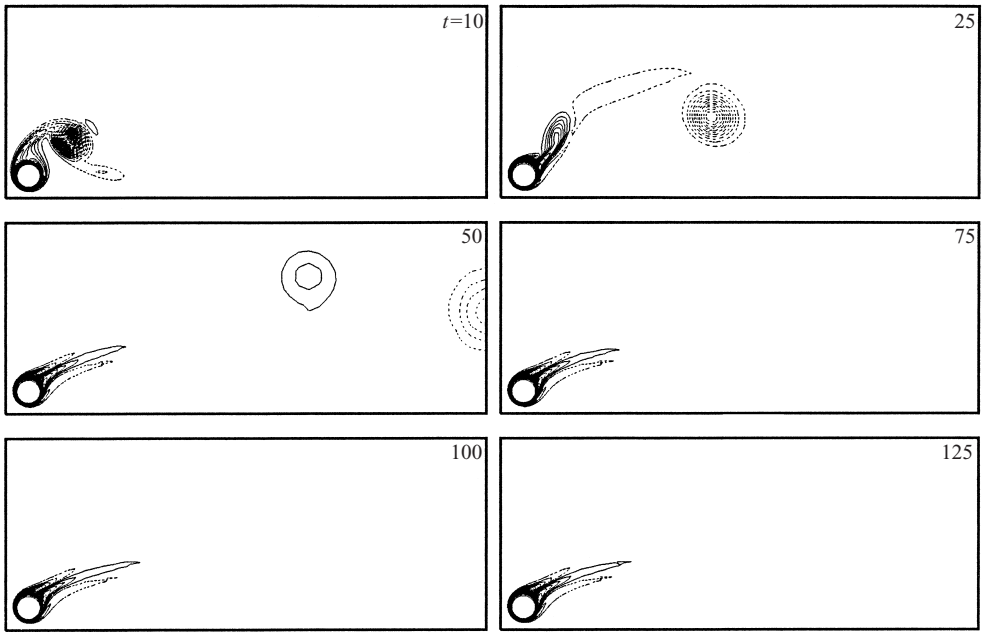

FIGURE 12. $Re = 200$, $\alpha = 3.25$ flow past a rotating cylinder: vorticity field at various time instants.

observed for t as large as 50. However, at later time no new vortices are shed and the older ones are advected away from the cylinder.

4.1.6. *The second region of instability*

With an increase in spin rate the vorticity distribution near the cylinder shows very interesting patterns. This can be observed in figures 6, 7 and 8. For low rotation rates (for example, $\alpha = 0.5$) the vorticity distribution is quite similar to that for flow past a non-rotating cylinder. Negative (clockwise) vorticity is released in the wake from the upper surface while positive vorticity is released from the lower surface of the cylinder. For higher rotation rates, the vorticity is dragged with the cylinder and the positive and negative vorticity are wrapped around each other giving the appearance of tightly wound spirals. For $\alpha = 4.0$, in the near wake, the positive vorticity lies above the negative vorticity. To an observer who is far away from the cylinder, it may appear as if the upper surface releases positive vorticity in the wake while negative vorticity is released from the lower surface.

For $\alpha \sim 4.4$ the flow becomes unstable again and vortex shedding resumes. This is evident from the time histories of C_L, and the phase diagrams of C_L vs. C_D shown in figures 2 and 5. Only counter-clockwise rotating (positive) vortices are shed. This is quite different from the shedding for $\alpha = 0$ where both positive and negative vortices are shed, alternately. Figure 13 shows the vorticity fields at five instants during one vortex shedding cycle for $\alpha = 0$ and $\alpha = 4.5$. For $\alpha = 0$ the positive vortex grows in size pushing the negative vortex further away from the cylinder. Eventually, the vortex sheet that feeds the negative vortex pinches off and it is shed in the wake to be advected by the flow. Later, the negative vortex, fed by the vorticity from the upper surface of the cylinder grows in size while a positive vortex from the lower surface is shed. The alternate shedding of the two vortices forms one cycle of the variation of the lift force experienced by the cylinder. For $\alpha = 4.5$, the regions of

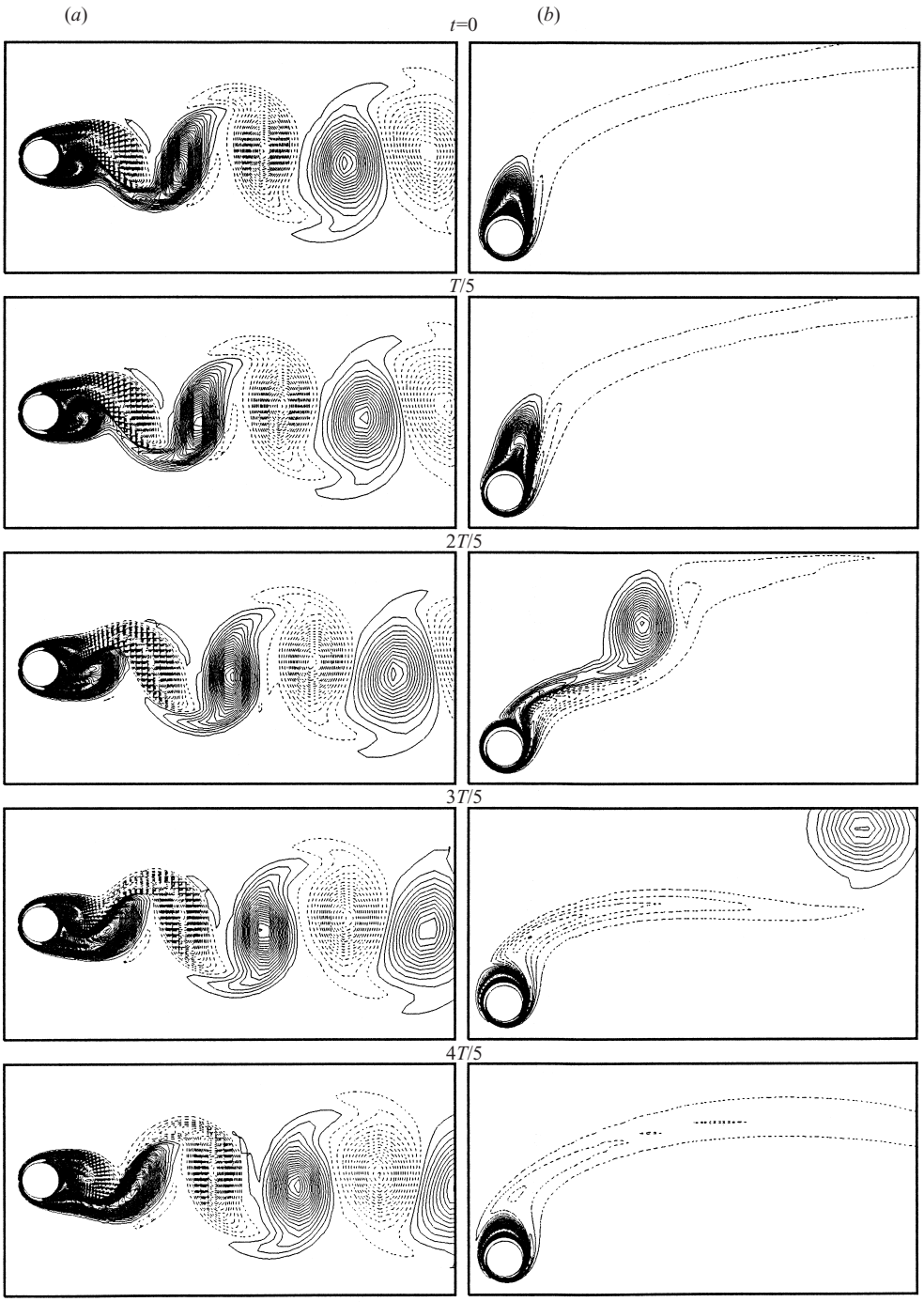

FIGURE 13. $Re = 200$ flow past a rotating cylinder: vorticity field for the fully developed solution at five instants during one vortex shedding cycle for $\alpha = 0$ (a) and $\alpha = 4.5$ (b).

positive and negative vorticity are wound around the cylinder surface. A positive vortex starts to develop close to the upper surface of the cylinder. As it grows in size it moves outward, away from the cylinder. This blocks the movement of the negative vortex around the cylinder surface, causing it to grow as well. Eventually, the positive vortex is shed and a new one starts to grow close to the cylinder. Unlike the positive vorticity, the negative vorticity is quite weak by the time it reaches the outer flow. Only one vortex is shed during each cycle of the time variation of the lift coefficient. This instability is limited to a very narrow region of α and the flow is stable, again, for $\alpha > 4.8$. The Strouhal number during this second region of instability is quite small compared to that seen for $\alpha < 2$. However, the r.m.s. values of the unsteady components of the aerodynamic coefficients are quite high.

4.1.7. *Multiple solutions for* $\alpha \geqslant 4.8$

All the solutions reported in the present article have been carried out using either the unsteady or steady Navier–Stokes equations. The computations with the steady Navier–Stokes equations require a good initial guess from the point of view of convergence of the nonlinear iterations. First, the steady-state solution for $Re = 200$ and $\alpha = 0$ is computed. This is used as an initial guess for computing the flow for $\alpha = 0.5$, which is used, in turn, to calculate the solution for $\alpha = 1.0$, and so on. Some of the solutions computed with the steady-state equations (increasing α) are shown in figure 8(*a*).

The computations with the unsteady Navier–Stokes equations begin with an initial condition that corresponds to an impulsive start. It is observed that for certain values of α, the flow achieves a steady state. The vorticity fields for some of the solutions are shown in figures 6 and 7. It is observed from figures 6 and 8(*a*) that the solutions for the $\alpha = 5$ flow from the steady (computations with increasing α) and unsteady (computations following an impulsive start) computations are qualitatively different. Using the solution for $\alpha = 5$ from the unsteady computations steady-state flows are computed for lower α. The vorticity fields for these solutions computed via decreasing α are shown in figure 8(*b*). It is observed that the steady-state solutions for increasing and decreasing α are different for $\alpha \geqslant 4.8$. This is also reflected in the plots for the variation of the mean values of C_D and C_L with α as shown in figure 11. It will be shown, later in the article, that the solutions corresponding to increasing α for $\alpha \geqslant 4.8$ are unstable while the solutions for decreasing α are stable with respect to small disturbances.

4.2. *Linear stability analysis*

To add further confidence to the computations presented in the previous section, a global non-parallel flow stability analysis is carried out for the steady-state solutions. This is, perhaps, the first attempt to set up a finite element formulation with the SUPG and PSPG stabilizations to look at the stability of flows. To test the formulation and its implementation we first try to determine the Hopf bifurcation point for flow past a non-rotating cylinder.

4.2.1. *Stability analysis for* $\alpha = 0$

Steady-state results for various Reynolds numbers ($Re < 50$) are obtained for three different finite element meshes. Mesh I consists of 5224 nodes while Mesh II is more refined with 14 805 nodes. Mesh III, the finest in the present study, consists of 24 840 nodes and 24 500 elements. The point of onset of instability of the flow is marked by

Researcher(s)	Re_c	St_c	Method	Grid size
Berger & Wille (1972)	50.00	0.12	Experiments	
Gresho *et al.* (1984)	50.00	0.14	Two-dimensional simulation, FEM	1825
Jackson (1987)	45.403	0.13 626	FEM with inverse iteration method	3056
Zebib (1987)	39–43	0.11–0.13	Standard eigenvalue method	
Williamson (1989)	47.90	0.1220	Experiments	
Morzynski & Thiele (1991)	46.270	0.13 451	FDM	3200
Norberg (1994)	47.4 ± 0.5	0.1177	Experiments	
Morzynski *et al.* (1999)	47.00	0.1320	FEM with subspace iteration method	15 838
Ding & Kawahara (1999)	46.389	0.12 619	FEM with Arnoldi's method	9870
Present paper (Mesh I)	48.2	0.1202	FEM with subspace iteration method	5224
Present paper (Mesh II)	47.5	0.1189	FEM with subspace iteration method	14 805
Present paper (Mesh III)	47.4	0.1169	FEM with subspace iteration method	24 840

TABLE 2. Hopf bifurcation for uniform flow past a non-rotating cylinder: comparison of the critical parameters.

the real part of the eigenvalue λ_r becoming positive. Results from the present method are compared with those reported by other researchers in table 2.

From table 2 it is seen that the results from the present formulation are in very good agreement with the experiments of Williamson (1989) and Norberg (1994). Further, of all those listed in the table, the present results with Mesh III give the closest match with the critical Reynolds and Strouhal numbers found from their experiments. The vorticity and pressure fields for the steady-state solution along with the vorticity fields for the real and imaginary parts of the unstable eigenmode close to the onset of instability, computed with Mesh III, are shown in figure 14. Also shown in the same figure are the vorticity fields for an instantaneous solution from the 2D DNS (two-dimensional direct numerical simulation) and by combining the steady-state solution and the most unstable eigenmode. The two solutions look very similar, at least, in the near wake. To obtain a closer match to the two-dimensional DNS results, one should include a larger number of eigenmodes. This method will work only for $Re \sim Re_c$ when the perturbations to the steady-state solution are relatively small. These pictures are very similar to the ones reported by Ding & Kawahara (1999). The wake of the perturbed solution, as expected, consists of alternately rotating vortices. It is interesting to observe that although both the real and imaginary eigenmodes are symmetric about the cylinder axis the unsteady solution is not. This is because the vorticity field for the basic steady solution is anti-symmetric while that for the eigenmodes is symmetric. The combination of the basic solution and the perturbations due to the eigenmodes, therefore, results in a solution that is made up of alternately rotating vortices. It is also observed that the pressure and x-component of velocity fields for the steady-state solution are symmetric, while those for the eigenmodes are anti-symmetric. In addition, the y-component of velocity for the steady-state solution is anti-symmetric while it is symmetric for the eigenmodes.

4.2.2. *Stability analysis for the rotating cylinder*

The steady-state solutions obtained for $Re = 200$ and various values of α are analysed for their stability. The vorticity fields for some of the steady-state solutions were shown in figure 8. Recall that to investigate the stability of the fluid system we need to track the rightmost eigenvalue (λ). If the real part of this eigenvalue is positive, any perturbations to the flow will amplify, rendering the flow unstable.

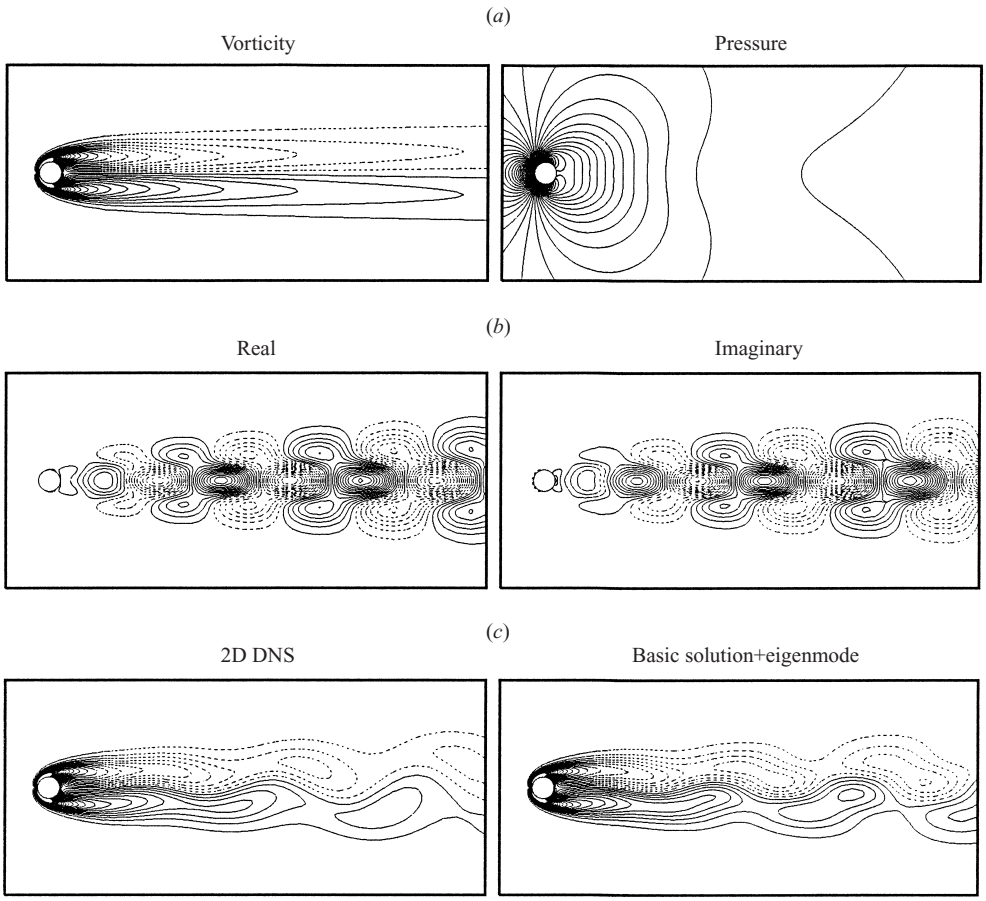

FIGURE 14. $Re = 48.1$ flow past a stationary cylinder: the steady and unsteady solutions and the most unstable eigenmode. (*a*) Steady-state solution, (*b*) real (left) and imaginary (right) parts of the vorticity field for the most unstable eigenmode, (*c*) vorticity fields for the unsteady solution obtained via two-dimensional DNS (left) and combining the steady-state solution and the most unstable eigenmode (right).

Because of a singularity in one of the coefficient matrices, we are restricted to tracking $1/\lambda$ (see § 3.2). Since the real parts of both λ and $1/\lambda$ have the same sign for assessing the onset of instability of a flow it suffices to track the rightmost value of either λ or $1/\lambda$. However, for α that is farther from the onset of instability a significantly larger effort is required to find the most unstable mode.

Figure 15 shows the variation, with α, of the real part of the rightmost λ. It is seen that λ_r is positive for $0 \leqslant \alpha \leqslant 1.90$ which implies that the steady flow is unstable in this regime. This observation is consistent with the one from the direct numerical simulations, presented earlier. The flow is stable for $1.91 \leqslant \alpha \leqslant 4.34$, signified by negative value of λ_r in this range. The flow becomes unstable again for $\alpha = 4.35$. The imaginary part of the most unstable eigenvalue is related to the Strouhal number of the flow, especially at the onset of instability. Figure 11 shows that for $\alpha = 1.91$ and 4.35 the St values from both the unsteady computations and linear stability analysis are identical. The vorticity fields for the real and imaginary parts of the most unstable eigenmode for $\alpha = 1.91$ and $\alpha = 4.37$ are shown in figure 16. For $\alpha = 1.91$ the wake

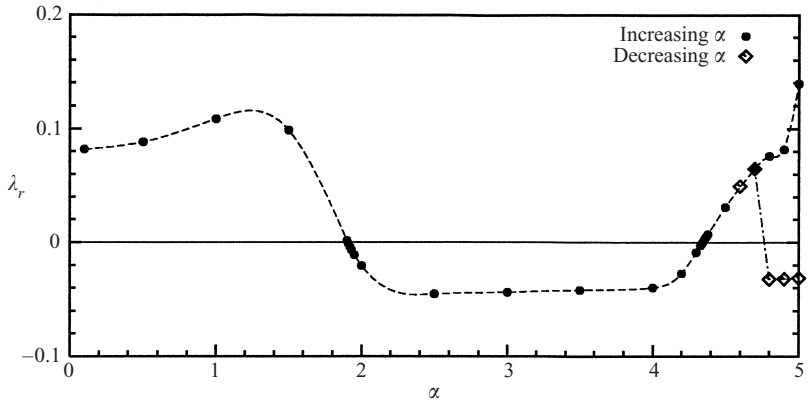

FIGURE 15. $Re = 200$ flow past a rotating cylinder: real part of the eigenvalue corresponding to the most unstable mode for the steady-state solutions.

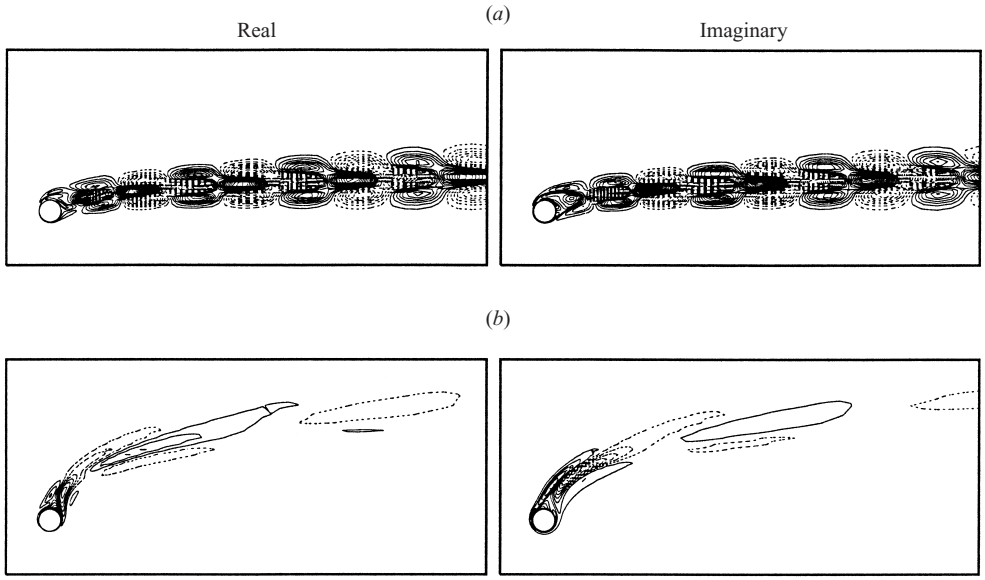

FIGURE 16. $Re = 200$ flow past a rotating cylinder: real and imaginary parts of the vorticity field for the most unstable mode for $\alpha = 1.91$ (a) and $\alpha = 4.37$ (b).

consists of a train of alternate positive and negative vortices which are of comparable strengths. This wake structure is quite similar to that observed for the non-rotating cylinder except for an upward deflection caused by the rotation of the cylinder. The tail of each vortex is engulfed by the one downstream of it. At $\alpha = 4.37$, there are fewer vortices in the wake. Some similarities can be observed between this figure and figure 13(b) for $\alpha = 4.5$ at $t = 2T/5$ and $3T/5$.

As pointed out in the previous section, multiple steady-state solutions are obtained for $\alpha \geqslant 4.8$. Depending on the initial guess/initial conditions for the computations, one of the two solutions can be realized. Solution 1 is obtained by increasing α by using the steady-state solution from lower α as an initial guess. Solution 2 results from unsteady computations that are initiated with an impulsive start. This is identical to the solution obtained using steady-state computations via decreasing α and starting

with the solution obtained for $\alpha = 5$ following an impulsive start. As can be seen from figure 15, solutions on the branch with decreasing α are stable while those on the branch with increasing α are unstable. When the unstable steady-state solution for $\alpha = 5$ is used as an initial condition to continue the unsteady computations a vortex is shed and the solution settles to the stable one. This is also in line with the observation made in Mittal (2001*b*) where the stability of the flow for $\alpha = 5$ was checked by introducing eccentricity/wobble in the motion of the cylinder. It was found that the mean solution for the eccentrically rotating cylinder is quite similar to that when the centre of rotation lies at the geometric centre of the cylinder. It is interesting to note that the solutions on the increasing α branch are similar to the steady-state solutions for lower α (for example, $\alpha = 4.7$) which are also unstable.

4.2.3. *A possible cause for the second instability*

The vorticity is created on the surface of the cylinder because of the no-slip condition on velocity. It is transported to other locations in the flow via advection and diffusion. Closed streamlines are formed around the cylinder surface for $\alpha > 2$. The strength of vorticity generated on the cylinder surface increases with increase in α. This increase is accompanied by a thicker region of closed streamlines around the cylinder surface. In such a situation, in steady flow, it is the diffusion mechanism that is responsible for transporting the vorticity to the outer flow. Vortex shedding cannot occur if vorticity of sufficient strength is unable to diffuse to the flow outside the closed streamlines.

Figure 17 shows the streamlines for the steady-state solutions for $\alpha = 4$, 4.5 and 5.0. Both the stable (decreasing α) and unstable (increasing α) solutions for $\alpha = 5$ are shown. The thick solid lines represent the set of points where the negative vorticity is maximum at a given radial distance from the centre of the cylinder. The thick broken lines show the same for positive vorticity. The cross symbols show the location of the stagnation point in the flow. The vorticity decreases as one moves away from the cylinder along the solid line. For $\alpha = 5$, in the case of stable flow, the vorticity decays to a very low level (thick lines are plotted only for magnitude of vorticity exceeding 0.2) before it can reach the outer flow beyond the closed streamlines. For $\alpha = 4.0$, the vorticity does diffuse to the outer flow. However, most of it is advected by high-speed flow. On the other hand, for $\alpha = 4.5$, while the negative vorticity is again advected by the high-speed flow, the positive vorticity is fed to a region close to the stagnation point. In an unsteady situation, in the event of a perturbation to the steady flow, the balance between the advection and diffusion of vorticity is disturbed. Since the flow, close to the stagnation point, moves quite slowly vorticity may build up with time. Eventually, this leads to vortex shedding. This is consistent with the observation that for $\alpha = 4.5$, only positive vortices are shed. The steady-state unstable flow for $\alpha = 5$ is also associated with the feeding of positive vorticity of significant strength to fluid close to the stagnation point. When this flow is used as an initial condition for unsteady computations and round-off errors perturb the flow, it is observed that a positive vortex is shed from the cylinder and the flow settles to the stable state.

We have observed that the wake region, consisting of slowly moving fluid, behind a stationary cylinder is quite large. It shrinks in size as the spin rate of the cylinder increases. Close to $\alpha = 4.4$ the region of slowly moving fluid starts to increase again. Vortex shedding occurs only if vorticity of large enough strength is released in a region of slowly moving, preferably, recirculating fluid.

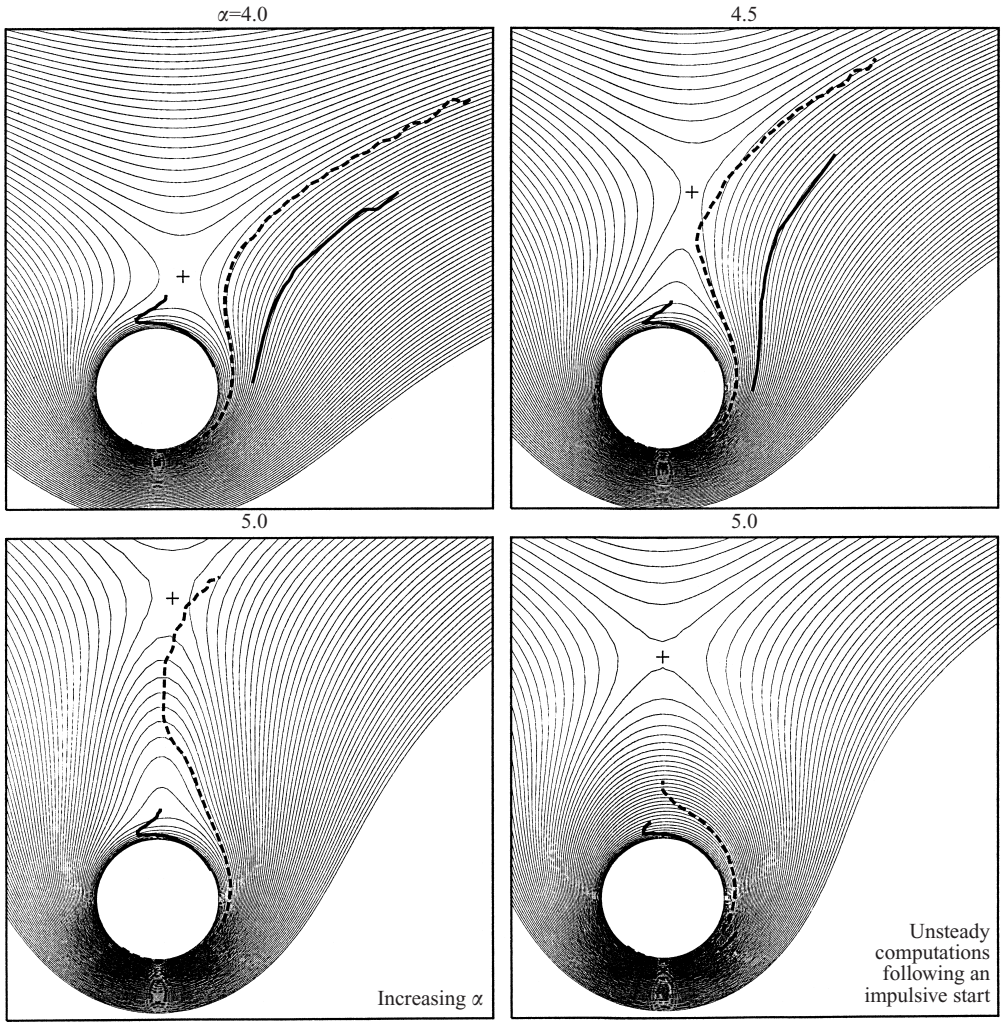

FIGURE 17. $Re = 200$, $\alpha = 4.0$, 4.5 and 5.0 flow past a rotating cylinder: streamlines for the steady-state flow. The thick solid lines show the points which have maximum value of negative vorticity (magnitude larger than 0.2) at each radial location while the thick broken ones denote the same for positive vorticity. The cross denotes the location of the stagnation point.

4.2.4. C_L *for large rotation rates*

Very high lift coefficients are observed for high rotation rates of the cylinder. Researchers in the past have reported varied results on the magnitude of lift that can be generated via the Magnus effect. Goldstein (1938), based on intuitive arguments by Prandtl, suggests that the maximum value of the lift coefficient that can be generated by a spinning cylinder is 4π (~ 12.6). Chew *et al.* (1995) have reported that their computations are in agreement with Prandtl's postulate. They find that for $Re = 1000$, the estimated mean lift coefficient approaches asymptotic values with increase in α. However, Tokumaru & Dimotakis (1993) have reported values of lift coefficient, from their laboratory experiments, that have exceeded this limit. According to them, the unsteady effects weaken Prandtl's hypothesis and the three-dimensional/end effects are responsible for lowering the value of lift coefficient that could be achieved in a

purely two-dimensional flow. The present results are in good agreement with those from the high-α theory proposed by Glauert (1957). Recently, Stansby & Rainey (2001) have reported two-dimensional computational results for flow past a spinning cylinder for $Re = 200$. They also find that as the rotation rate increases, C_L approaches the value predicted by potential flow theory ($C_L = 2\pi\alpha$). The present results support the observation by Tokumaru & Dimotakis (1993) that Prandtl's limit may not hold for large aspect ratio cylinders. It certainly does not hold for the two-dimensional flows.

Our preliminary computations for three-dimensional flows show that the aspect ratio of the cylinder and its end conditions (spanwise length/diameter) play an important role in determining the amount of lift generated by the rotating cylinder. A no-slip sidewall (no end plates) results in flow separation. In addition, the entire span is associated with centrifugal instabilities. Both these effects contribute to loss of lift and increased drag compared to a purely two-dimensional flow. These results will be presented in a future paper.

5. Concluding remarks

Flow past a cylinder, rotating in the counter-clockwise sense, and placed in uniform stream ($Re = 200$) has been analysed for various spin rates ($0 \leqslant \alpha \leqslant 5$). A stabilized finite element method is utilized to solve the incompressible Navier–Stokes equations in the primitive variables formulation. The flow is extremely complex and is associated with both two- and three-dimensional instabilities.

For $0 \leqslant \alpha \leqslant 1.9$ a von Kármán street is seen in the wake behind the cylinder. For non-zero α the vortex street is deflected away from the centre line. The wake becomes narrower and the Strouhal number for vortex shedding decreases with increase in rotation rate. Vortex shedding ceases beyond $\alpha \sim 1.9$. However, it takes quite a long time for the flow to develop to the final solution following an impulsive start. It is for this reason that some researchers, in the past, concluded from their simulations that the flow at $\alpha = 3.25$ is associated with vortex shedding. The present results show that the flow achieves a steady state for $\alpha = 3.25$. At high rotation rates it is seen that the lift for purely two-dimensional flows can be very large. The values of the lift coefficient obtained in the present work exceed the maximum limit based on the arguments of Prandtl.

The vorticity distribution around the cylinder goes through certain interesting changes with increase in α. For high α the vorticity generated on the cylinder surface is dragged along with it. The positive and negative vorticity appear as tightly wound spirals. The flow remains stable for $1.91 \leqslant \alpha \leqslant 4.34$ but loses its stability again for $\alpha \sim 4.35$. For this rotation rate, unlike the shedding for lower α, the cylinder sheds vortices of counter-clockwise sense only from its lower surface. Vortex shedding continues for higher spin rates and the flow becomes stable, yet again, for $\alpha \geqslant 4.8$.

Solutions are also computed for various α by dropping the unsteady terms from the governing equations. The stability of these solutions is analysed by conducting a global, non-parallel linear stability analysis. The implementation of the formulation is validated by locating the Hopf bifurcation for flow past a non-rotating cylinder. The results are in very good agreement with those from other studies. Next, the stability of the steady flows for a spinning cylinder is analysed. The regions of stability (and instability) from this study are in excellent agreement with those from the two-dimensional direct numerical simulations. The Strouhal numbers, corresponding to

the vortex shedding frequency, for $\alpha = 1.91$ and 4.35 where the flow is barely unstable also match with the DNS.

A possible cause for this interesting behaviour of flow stability (or instability) is proposed. The strength of vorticity generated on the cylinder surface increases with the increase in spin rate. This is accompanied by an increase in the thickness of the region with closed streamlines around the cylinder. For vortex shedding to occur, vorticity of large enough strength must be carried to the outer flow, outside closed streamlines, via diffusion. This region of vorticity, in the outer flow, must also be a sufficiently large area of slowly moving, preferably recirculating, fluid. Under these conditions the vorticity can pile up in a certain region of the flow and vortex shedding can take place. For $\alpha = 0$ a large region behind the cylinder is associated with slowly moving fluid. The size of this region reduces, rapidly, with increase in spin rate. This explains the disappearance of vortex shedding for $\alpha \sim 2.0$. However, for $\alpha \sim 4.5$, the region of slowly moving fluid increases again and this region is also associated with significantly high positive vorticity. Vortex shedding re-occurs in a narrow range of α. For larger rotation rates (for example, $\alpha \sim 5$) the vorticity is restricted to the region of flow around the cylinder with closed streamlines, resulting in a stable flow.

Two steady-state solutions are seen for $\alpha \geqslant 4.8$: one is unstable while the other is stable. The solution obtained via unsteady computations following an impulsive start is stable. The unstable solution resembles the steady-state solution for $\alpha = 4.7$ which is itself unstable.

The present work has significant implications for the flow control strategies that utilize rotating cylinder elements. It would be undesirable to use $\alpha < 2$ and $4.3 < \alpha < 4.8$ because the flow is unstable. For other spin rates, even though vortex shedding does not occur, one can expect centrifugal instabilities along the entire span of the rotating cylinder. In addition, the end effects are expected to be important for low-aspect-ratio cylinders.

Partial support for this work has come from the Department of Science and Technology, India.

REFERENCES

Badr, H. M., Coutanceau, M., Dennis, S. C. R. & Menard, C. 1990 Unsteady flow past a rotating cylinder at Reynolds numbers 10^3 and 10^4. *J. Fluid Mech.* **220**, 459–484.

Badr, H. M. & Dennis, S. C. R. 1985 Time-dependent viscous flow past an impulsively started rotating and translating circular cylinder. *J. Fluid Mech.* **158**, 447–488.

Berger, E. & Wille, R. 1972 Periodic flow phenomena. *Annu. Rev. Fluid Mech.* **4**, 313–340.

Chang, C. C. & Chern, R. L. 1991 Vortex shedding from an impulsively started rotating and translating circular cylinder. *J. Fluid Mech.* **233**, 265–298.

Chen, Y.-M. Ou, Y.-R. & Pearlstein, A. J. 1993 Development of the wake behind a circular cylinder impulsively started into rotary and rectilinear motion. *J. Fluid Mech.* **253**, 449–484.

Chew, Y. T., Cheng, M. & Luo, S. C. 1995 A numerical study of flow past a rotating circular cylinder using a hybrid vortex scheme. *J. Fluid Mech.* **299**, 35–71.

Chou, M.-H. 2000 Numerical study of vortex shedding from a rotating cylinder immersed in a uniform flow field. *Intl J. Numer. Meth. Fluids* **32**, 545–567.

Coutanceau, M. & Menard, C. 1985 Influence of rotation on the near-wake development behind an impulsively started circular cylinder. *J. Fluid Mech.* **158**, 399–446.

Degani, A. T., Walker, J. D. A. & Smith, F. T. 1998 Unsteady separation past moving surfaces. *J. Fluid Mech.* **375**, 1–38.

Diaz, F., Gavalda, J., Kawall, J. G., Keller, J. F. & Giralt, F. 1983 Vortex shedding from a spinning cylinder. *Phys. Fluids* **26**, 3454–3460.

Ding, Y. & Kawahara, M. 1999 Three-dimensional linear stability analysis of incompressible viscous flows using the finite element method. *Intl J. Numer. Meth. Fluids* **31**, 451–479.

Glauert, W. B. 1957 The flow past a rapidly rotating circular cylinder. *Proc. R. Soc. Lond.* A **242**, 108–115.

Goldstein. S. 1938 *Modern Developments in Fluid Dynamics.* Clarendon.

Gresho, P. M., Chan, S. T., Lee, R. L. & Upson, C. D. 1984 A modified finite element method for solving the time-dependent incompressible Navier–Stokes equations. Part 2. Applications. *Intl J. Numer. Meth. Fluids* **4**, 619.

Hu, G., Sun, D., Yin, X. & Tong, B. 1996 Hopf bifurcation in wakes behind a rotating and translating circular cylinder. *Phys. Fluids* **8**, 1972–1974.

Jackson, C. P. 1987 A finite-element study of the onset of vortex shedding in flow past variously shaped bodies. *J. Fluid Mech.* **182**, 23–45.

Jaminet, J. F. & Van Atta, C. W. 1969 Experiments on vortex shedding from rotating circular cylinders. *AIAA J.* **7**, 1817–1819, 1969.

Kang, S. & Choi, H. 1999 Laminar flow past a rotating cylinder. *Phys. Fluids* **11**, 3312–3320.

Kimura, T. & Tsutahara, M. 1991 Wake of a rotating circular cylinder. *AIAA J.* **30**, 555–556.

Mittal, S. 1992 Stabilized space-time finite element formulation for unsteady incompressible flows involving fluid–body interaction. PhD thesis, University of Minnesota.

Mittal, S. 2000 On the performance of high aspect ratio elements for incompressible flows. *Comput. Meth. Appl. Mech. Engng* **188**, 269–287.

Mittal, S. 2001*a* Control of flow past bluff bodies using rotating control cylinders. *J. Fluids Struct.* **15**, 291–326.

Mittal, S. 2001*b* Flow past rotating cylinders: Effect of eccentricity. *Trans. ASME: J. Appl. Mech.* **68**, 543–552.

Modi, V. J. 1997 Moving surface boundary-layer control: A review. *J. Fluids Struct.* **11**, 627–663.

Modi, V. J., Mokhtarian, F. & Fernando, M. S. U. K. 1991 Moving surface boundary-layer control as applied to two-dimensional airfoils. *J. Aircraft* **28**, 104–112.

Morzynski, M., Afanasiev, K. & Thiele, F. 1999 Solution of the eigenvalue problems resulting from global non-parallel flow stability analysis. *Comput. Meth. Appl. Mech. Engng* **169**, 161–176.

Morzynski, M. & Thiele, F. 1991 Numerical stability analysis of a flow about a cylinder. *Z. Angew. Math. Mech.* **71**, T424–T428.

Norberg, C. 1994 An experimental investigation of the flow around a circular cylinder: influence of aspect ratio. *J. Fluid Mech.* **258**, 287–316.

Prandtl, L. 1925 The Magnus effect and windpowered ships. *Naturwissenschaften* **13**, 93–108.

Saad, Y. & Schultz, M. 1986 GMRES: A generalized minimal residual algorithm for solving nonsymmetric linear systems. *SIAM J. Sci. Statist. Comput.* **7**, 856–869.

Stansby, P. K. & Rainey, R. C. T. 2001 A CFD study of the dynamic response of a rotating cylinder in a current. *J. Fluids Struct.* **15**, 513–521.

Stewart, G. W. 1975 Methods of simultaneous iteration for calculating eigenvectors of matrices. In *Topics in Numerical Analysis II* (ed. J. H. H. Miller), pp. 169–185. Academic.

Tezduyar, T. E., Mittal, S., Ray, S. E. & Shih, R. 1992 Incompressible flow computations with stabilized bilinear and linear equal-order-interpolation velocity-pressure elements. *Comput. Meth. Appl. Mech. Engng* **95**, 221–242.

Tokumaru, P. T. & Dimotakis, P. E. 1991 Rotary oscillation control of cylinder wake. *J. Fluid Mech.* **224**, 77–90.

Tokumaru, P. T. & Dimotakis, P. E. 1993 The lift of a cylinder executing rotary motions in a uniform flow. *J. Fluid Mech.* **255**, 1–10.

Van Atta, C. W. 1997 Comments on "Hopf bifurcation in wakes behind a rotating and translating circular cylinder" [Phys. Fluids 8, 1972 (1996)]. *Phys. Fluids* **9**, 3105–3106.

Williamson, C. H. K. 1989 Oblique and parallel modes of vortex shedding in the wake of a circular cylinder at low Reynolds numbers. *J. Fluid Mech.* **206**, 579–627.

Williamson, C. H. K. 1991 2-D and 3-D aspects of the wake of a cylinder, and their relation to wake computations. In *Lectures in Applied Mathematics* (ed. C. R. Anderson & C. Greengard), vol. 28, pp. 719–751. American Mathematical Society.

Zebib, A. 1987 Stability of viscous flows past a circular cylinder. *J. Engng Maths* **21**, 155–165.